UNIVERSIDADE ESTADUAL PAULISTA "JÚLIO DE MESQUITA FILHO"
CÂMPUS DE ILHA SOLTEIRA

LUCAS SIMON ARAÚJO

DYNAMIC MODE DECOMPOSITION FOR DATA-DRIVEN MODELING OF SPATIO-TEMPORAL DYNAMICS

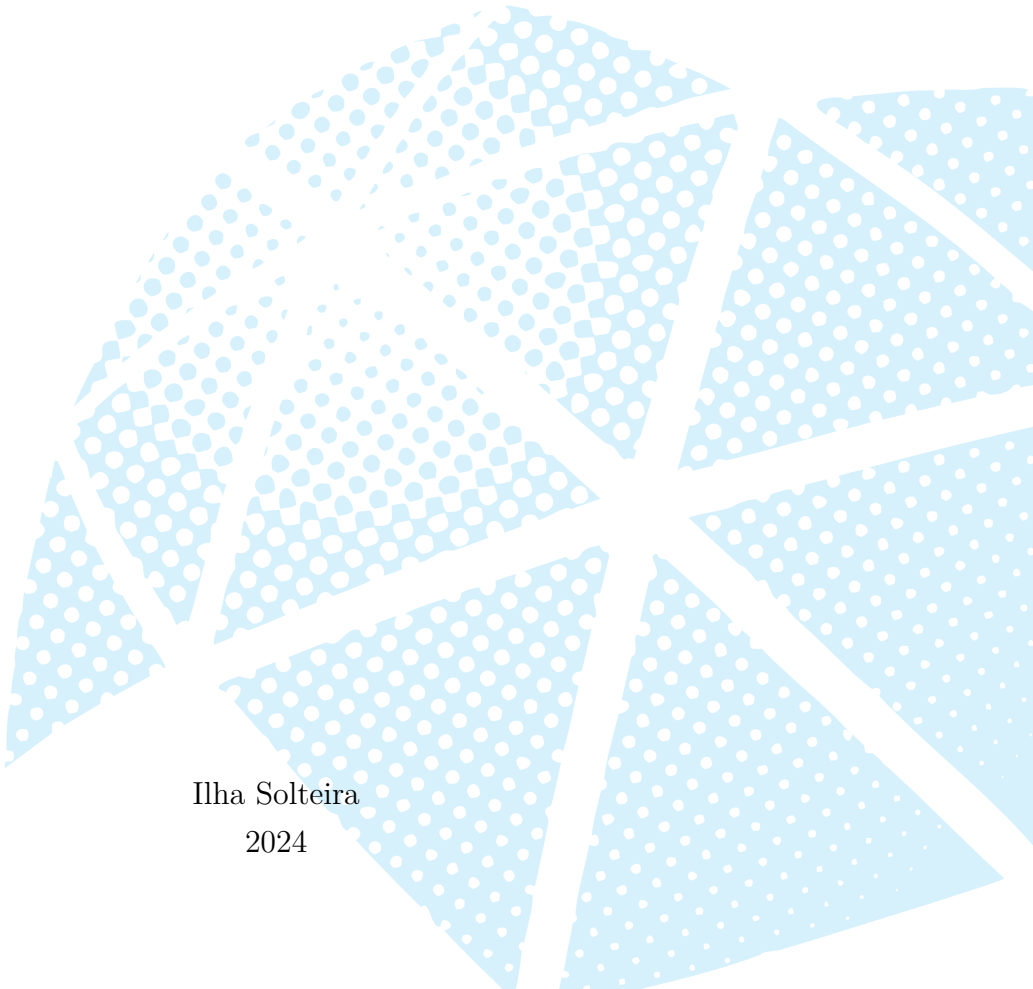

Ilha Solteira
2024

UNIVERSIDADE ESTADUAL PAULISTA
"JÚLIO DE MESQUITA FILHO"
Campus de Ilha Solteira

LUCAS SIMON ARAÚJO

DYNAMIC MODE DECOMPOSITION FOR DATA-DRIVEN MODELING OF SPATIO-TEMPORAL DYNAMICS

Dissertation presented to the São Paulo State University (Unesp), School of Engineering, Ilha Solteira, as part of the requirements for obtaining the MSc. degree in Mechanical Engineering.

Knowledge Area: Solid Mechanics.

Prof. Dr. Americo Barbosa da Cunha Junior
Supervisor

Ilha Solteira
2024

FICHA CATALOGRÁFICA
Desenvolvido pelo Serviço Técnico de Biblioteca e Documentação

A663d

Araújo, Lucas Simon.
Dynamic mode decomposition for data-driven modeling of spatio-temporal dynamics / Lucas Simon Araújo. -- Ilha Solteira: [s.n.], 2024
57 f. : il.

Dissertação (mestrado) - Universidade Estadual Paulista. Faculdade de Engenharia de Ilha Solteira. Área de conhecimento: Mecânica dos Sólidos, 2024

Orientador: Americo Barbosa da Cunha Junior

Inclui bibliografia

1. Sistemas dinâmicos não-lineares. 2. Operador de Koopman. 3. Decomposição em modos dinâmicos. 4. Modelagem orientada por dados.

Amanda Sertori dos Santos
Bibliotecária - CRB/8-9061
Seção Técnica de Referência, Atendimento ao Usuário e Documentação
Diretoria Técnica de Biblioteca e Documentação

UNIVERSIDADE ESTADUAL PAULISTA

Câmpus de Ilha Solteira

CERTIFICADO DE APROVAÇÃO

TÍTULO DA DISSERTAÇÃO: DYNAMIC MODE DECOMPOSITION FOR DATA-DRIVEN MODELING OF SPATIO-TEMPORAL DYNAMICS

AUTOR: LUCAS SIMON ARAUJO

ORIENTADOR: AMERICO BARBOSA DA CUNHA JUNIOR

Aprovado como parte das exigências para obtenção do Título de Mestre em Engenharia Mecânica, área: Mecânica dos Sólidos pela Comissão Examinadora:

gov.br Documento assinado digitalmente
AMERICO BARBOSA DA CUNHA JUNIOR
Data: 29/07/2024 12:06:58-0300
Verifique em https://validar.iti.gov.br

Prof. Dr. AMERICO BARBOSA DA CUNHA JUNIOR (Participaçao Virtual)
Instituto de Matemática e Estatística / Universidade do Estado do Rio de Janeiro - UERJ

gov.br Documento assinado digitalmente
FERNANDA THAIS COLOMBO
Data: 29/07/2024 12:18:41-0300
Verifique em https://validar.iti.gov.br

Dra. FERNANDA THAÍS COLOMBO (Participaçao Virtual)
Departamento de Engenharia Mecânica / Faculdade de Engenharia de Ilha Solteira

ICP Brasil Documento assinado digitalmente
MARCELA RODRIGUES MACHADO
Data: 29/07/2024 12:48:47-0300
Verifique em https://validar.iti.gov.br

Profa. Dra. MARCELA RODRIGUES MACHADO (Participaçao Virtual)
Departamento de Engenharia Mecânica / Universidade de Brasília - UnB

gov.br Documento assinado digitalmente
ADRIANO TODOROVIC FABRO
Data: 29/07/2024 15:45:36-0300
Verifique em https://validar.iti.gov.br

Prof. Dr. ADRIANO TODOROVIC FABRO (Participaçao Virtual)
Departamento de Engenharia Mecânica / Universidade de Brasília - UnB

Ilha Solteira, 29 de julho de 2024

ACKNOWLEDGEMENTS

I thank God for being my prop and source of purpose in this journey, blessing me with good people when I most needed.

I am grateful for all the friendships I made, with amazing people who helped me by sharing their experiences. Some of them: Afonso Nunes, Eduardo Preto, Henrique Novais, Fernanda Colombo, Estênio Fuzzaro, Estêvão Fuzzaro, Renan Cavenaghi, Wellington Nogueira, João Pedro Noremberg, Diogo Karmouche.

I would like to extend my gratitude to Professor Samuel da Silva for his assistance, along with his notably team, which welcomed me to FEIS-UNESP. From this team I highlight the substantial contribution of Eduardo Preto, who made the experiment of aluminum plate temperature field possible.

It is important to recognize the essential role of Joselaine Seleguini and Bruno Arakaki, who treated my anxiety with professionalism.

I am very grateful to my advisor Americo Cunha Jr, who I already esteemed as an amazing researcher and professor, and now I also admire for the person he is. Thank you for your guidance and patience.

A special thanks to my support network with my parents Adriane and Sérgio, my brother Vitor, and also my soon fiancee Luana for their unconditional love, which maintained me stand up against the troubles.

This study was financed in part by the Coordenação de Aperfeiçoamento de Pessoal de Nível Superior - Brasil (CAPES) - Finance Code 001.

"Hoje me sinto mais forte, mais feliz quem sabe
Só levo a certeza de que muito pouco sei
Ou nada sei."
(Tocando em frente - Renato Teixeira e Almir Sater)

ABSTRACT

Nonlinear phenomena are almost ubiquitous in many different engineering applications. Their underlying nonlinearities bring extra complexity to characterize, predict, and control systems. There are two standard ways to deal with this challenge: through linearization, which restricts the response; and through a nonlinear perspective, which in turn increases the analysis complexity. Still in 1931, Koopman had already proposed a third way, expanding the set of states to encompass the nonlinearities inside a Hilbert space. Towards approximate the Koopman operator, we have explored an up-and-coming technique called dynamic mode decomposition (DMD), which has been bringing attention in the last decades, especially in the fluid dynamics community. The theoretical foundations of both Koopman and DMD theories are explained, including the development of the basic algorithm. In order to challenge the performance of DMD reconstruction, four optimization benchmark functions are used to generate complex dynamic field data as input for the algorithm. Their reconstructions provide insights into the limitations of the method. In addition, a physical phenomenon is addressed in this work, the heat diffusion into a homogeneous, isotropic, and flat plate. The dynamical field is well recovered through analytically generated data by DMD with good accuracy even in the presence of noise and coarse spatial sampling. To complete the analysis, an experimental setup of an aluminum plate under a heat source is mounted and generate data for the DMD input, also getting good reconstruction results.Beyond the reconstructions, the algorithm also provided the modes, frequencies, and an approximation for the Koopman operator, useful results for identification and control. For all the cases studied, the reconstructions are compared with the original data using similarity analysis for a range of truncation levels, promoting a discussion of how this parameter influences the accuracy of the reconstruction. The results confirm the ability of DMD to extract spatio-temporal patterns and recover these original fields with high similarity even using a reduced dimensionality, which corroborates the literature by highlighting DMD as a promising tool for studying dynamic systems, especially those whose governing equations are not sufficiently known.

Keywords: Nonlinear dynamical systems; Koopman operator; Dynamic Mode Decomposition; Data-driven Modeling.

RESUMO

Os fenômenos não lineares são quase onipresentes em diversas aplicações de engenharia. Suas não-linearidades inerentes trazem complexidade adicional para caracterizar, prever e controlar sistemas. Há duas formas tradicionais de lidar com este desafio: a linearização, que restringe a resposta; e por uma abordagem não linear, que, por sua vez, dificulta a análise. Ainda em 1931, Koopman propôs uma terceira via, mediante uma expansão no espaço de estados para compreender as não linearidades dentro de um espaço de Hilbert. Para aproximar o operador de Koopman, exploramos uma técnica emergente chamada decomposição de modos dinâmicos (DMD), que vem ganhando destaque nas últimas décadas, especialmente na comunidade de dinâmica dos fluidos. Os fundamentos teóricos das teorias Koopman e da DMD são explicados, incluindo o desenvolvimento básico do algoritmo. Com o objetivo de desafiar o desempenho da reconstrução DMD, quatro funções *benchmark* em problemas de otimização são utilizadas para gerar dados de campos dinâmicos complexos como entrada para o algoritmo. Suas reconstruções fornecem uma discussão acerca das limitações do método. Além disso, um fenômeno físico é abordado neste trabalho, a difusão de calor em uma placa plana homogênea e isotrópica. O campo dinâmico é bem recuperado através de dados gerados analiticamente pela DMD, mesmo na presença de ruído e amostragem espacial grosseira. Para completar a análise, uma configuração experimental de uma placa de alumínio sob uma fonte de calor é montada e gera dados reais para a DMD, obtendo uma boa reconstrução. Além das reconstruções, o algoritmo também forneceu os modos, frequências e uma aproximação para o operador de Koopman, resultados úteis para identificação e controle. Para todos os casos estudados as reconstruções são comparadas com os dados originais utilizando análise de similaridade para diferentes níveis de truncamento, promovendo uma discussão de como este parâmetro influencia na precisão do processo. Os resultados confirmam a capacidade da DMD em extrair padrões espaço-temporais e recuperar esses campos originais com alta similaridade mesmo com uma dimensionalidade reduzida, corroborando com a literatura ao destacar a DMD como uma ferramenta promissora para o estudo de sistemas dinâmicos, especialmente quando as equações governantes não são suficientemente conhecidas.

Palavras-chave: Sistemas Dinâmicos Não-lineares; Operador de Koopman; Decomposição em Modos Dinâmicos; Modelagem Orientada por Dados.

CONTENTS

1 INTRODUCTION

This chapter introduces the subject of this dissertation. In Section 1.1, the motivation for conducting this research is presented. Following that, Section 1.2 addresses the objectives of the work, while Section 1.3 discusses its achieved contributions. Finally, Section 1.4 outlines how the chapters are organized within this report.

1.1. MOTIVATION

Nonlinear phenomena are omnipresent across a wide spectrum of technological applications, manifesting in challenging operations like well drilling (Cunha Jr., 2015; Cunha Jr.; Soize; Sampaio, 2015; Lobo *et al.*, 2022; Ritto; Aguiar; Hbaieb, 2017; Ritto *et al.*, 2009), vibration analysis of slender structures (Facchinetti; Langre; Biolley, 2004; Kurushina; Pavlovskaia, 2018; Lopes, 2022), and seismic analysis for identifying potential reservoirs (Alves *et al.*, 2023; Emerick, 2018; Freitas *et al.*, 2021). The complexities introduced by nonlinearities pose significant hurdles in the characterization, prediction, and control of these phenomena.

The conventional strategy to address nonlinear dynamics has been through linearization, approximating the nonlinear system's response around an equilibrium point. Although this method simplifies analysis, it inherently limits the scope of the system's behavior it can capture, confined to narrow operational limits (Silva, 2022). Linearization, relying on a truncated Taylor series expansion and subsequent Jacobian matrix computation for systems with multiple state variables, offers a constrained view of a system's dynamics (Savi, 2017; Strogatz, 2014).

Alternatively, a nonlinear modeling approach employing tools like Poincaré maps, bifurcation diagrams, basins of attraction, and Lyapunov exponents offers a richer, more accurate analysis at the cost of increased complexity (Savi, 2017; Strogatz, 2014). This method has been gaining traction, as evidenced in (Kurushina; Pavlovskaia, 2018; Lopes; Peterson; Cunha Jr., 2019; Norenberg *et al.*, 2023; Reis *et al.*, 2024; Wang *et al.*, 2021).

In the early 20th century, Bernard Koopman introduced a groundbreaking perspective on analyzing nonlinear dynamical systems by describing their evolution through an operator acting on an infinite-dimensional Hilbert space. This method, centered around what is now known as the Koopman operator, offers a way to encapsulate the system's

dynamics in a linear framework, albeit not through linearization in the conventional sense. Instead, it provides a "global linearization" by detailing the flow of the system in its state space through a linear evolution equation (Koopman, 1931). In a nutshell, Koopman operator converts a finite dimension nonlinear system into an infinite dimension linear system. The philosophy of this approach is represented in Fig. 1.

Figura 1 – Transformation of a nonlinear dynamical system into a linear one trough the action of the Koopman Operator.

Source: Produced by the author.

For decades, the practical application of Koopman's theory remained a conceptual ideal, largely due to computational limitations. However, the advent of modern computational techniques and the growth of data availability enabled the emergence of data-driven modeling, revitalizing the interest in this approach (Brunton; Kutz, 2019). The fluid dynamics community spearheaded the revival of Koopman idea, with the pioneer work of Igor Mezić (Mezić; Banaszuk, 2004; Mezić, 2005; Mezić, 2013), followed by the contributions of Clarence Rowley (Rowley *et al.*, 2009), and Peter Schmid (Schmid, 2010; Schmid *et al.*, 2011), who set the basis for an Koopman operator approximation from spatio-temporal data via the so called Dynamic Mode Decomposition (DMD) (Budišić; Mohr; Mezić, 2012; Williams; Kevrekidis; Rowley, 2015).

DMD emerges as a particularly promising technique, offering a powerful lens for analyzing complex dynamical systems across fields as varied as fluid mechanics and epidemiology (Kutz *et al.*, 2016; Schmid, 2022). DMD's ability to identify spatio-temporal patterns from high-dimensional data and its modal decomposition capability make it a valuable tool for system characterization, prediction, and control (Kutz *et al.*, 2016; Proctor; Brunton; Kutz, 2016).

Recent explorations have applied DMD across diverse domains, including wind engineering (Li *et al.*, 2023), oscillating cylinder flow analysis (Ping *et al.*, 2021), and simulations of mesh refinement and density-driven gravity currents (Barros *et al.*, 2022; Barros; Cortes; Coutinho, 2020), to tumor growth models (Viguerie *et al.*, 2022). These applications highlight DMD's adaptability and its potential to complement classical modeling approaches (Brunton; Kutz, 2019; Gu *et al.*, 2024; Kaiser; Kutz; Brunton, 2021).

In essence, DMD represents a convergence of Singular Value Decomposition (SVD) and Fourier Transform (FT) techniques, offering a robust framework for dimensionality reduction and mode identification in complex systems (Golub; Loan, 2013; Kutz *et al.*, 2016). Due to these captivating abilities, we provided an immersion inside the DMD context with both theoretical foundation and hands-on applications to explore the method efficiency and along with its limitations.

A graphical abstract is elaborated and despicted in the Fig. 2, furnishing an overview of the dissertation's workflow. The upper block reveals the motivation presented in this section, with the data-driven modeling being an alternative branch for describing nonlinear complex dynamical systems, motivated by the growth in data availability and increase in computational power, where DMD is one special technique in this branch for leading with spatio-temporal systems. The middle block overviews the four prime steps of methodology, firstly the data generation through mathematical fields, Partial Differential Equations (PDEs), and experimental sensoring; followed by: pre-processing, DMD algorithm core, and post-processing. The bottom block express the main results, namely the fields reconstruction and extrapolation, the systems diagnosis with the modal decomposition, and a truncation analysis. The last block also present some practical applications that are enabled by the results presented, viz operational insights, control, and decision making.

1.2. OBJECTIVE

This study aims to introduce the reader to the DMD method by showing the theory; presenting its exact algorithm; and applying it to demonstrative examples with spatio-temporal data from analytical solution and experimental sensoring; beyond discussing how truncation influences the good reconstruction of data.

1.3. MAIN CONTRIBUTIONS

The key contributions of this dissertation are:

- Providing a review of the Koopman theory and dynamic mode decomposition with a pedagogical approach;

Figura 2 – Graphical abstract summarizing the dissertation's workflow. The first panel, in orange, explain the motivation; the second, in green, organize the information flux applied in the metodology; and the third panel, in purple, present some of the results achieved.

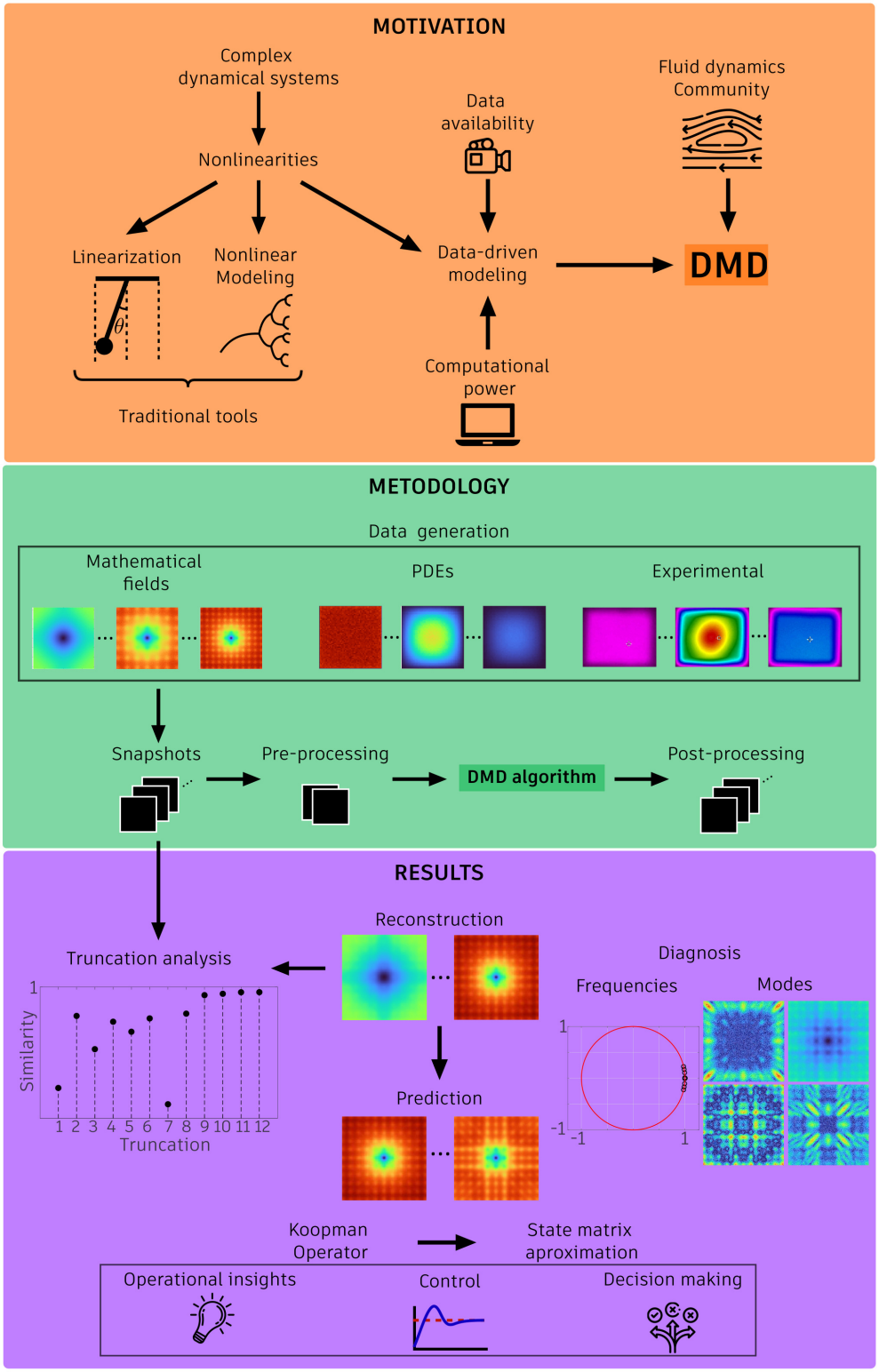

Source: Produced by the author.

- Developing and furnish the algorithm for all steps of DMD computation presented.
- Employing demonstrative examples of DMD reconstruction into analytical fields with noise added and poor spatial sampling;
- Applying the DMD technique in an experimental context to recover the thermal field of an aluminum plate under the action of a heat source;
- Revealing some limitations of the exact DMD algorithm by examination of reconstruction results;
- Exploring the truncation influence in the reconstruction using similarity analysis.

1.4. OUTLINE

The structure of this work spans six chapters:

Chapter 1: Introduction - Presents the study's motivation, objectives, and contributions.

Chapter 2: Koopman formalism for nonlinear dynamical systems - Develop a literature review around the Koopman methodology and explain the Koopman operator power of dealing with nonlinear dynamical systems.

Chapter 3: Dynamic mode decomposition - Delves into the novel approach used to approximate the Koopman operator, presenting the mathematical background along with its capabilities. Also introduce the DMD algorithm, with a detailed step-by-step explanation that culminates in a generalized algorithmic framework.

Chapter 4: Results and discussion - Firstly the data generation section is presented, consisting of three parts: data generated through four optimization benchmark functions, an analytical solution for the heat diffusion problem, and finally athwart an experiment generating real-world data. Next, showcases the singular values, modes, frequencies and reconstructions for the proposed examples. Likewise, the truncation influence in the reconstruction is studied throughout the cosine similarity measure between original and reconstructed data.

Chapter 5: Conclusions - Provides a concise overview of key findings and suggests directions for further research.

2 KOOPMAN FORMALISM FOR NONLINEAR DYNAMICAL SYSTEMS

In the beginning of last century, the success of infinite dimension operator-based formalism in the quantum mechanics (associated to Hilbert Theory), motivated its extension to another fields, like classical dynamical fields. In the face of the increasing of physics subsumed to this theory, Koopman (1931) developed a generalization accounting systems defining a steady n-dimensional flow. His theory is explained in the following section inside the dynamical systems context.

2.1. KOOPMAN OPERATOR

The dynamic systems of interest here are described by a differential equation of the form,

$$\frac{d\boldsymbol{x}}{dt} = f(\boldsymbol{x}, t, \mu)\,, \tag{2.1}$$

that translates its temporal variation as a function of the current state vector $\boldsymbol{x}(t) \in \mathbb{R}^n$, the continuous time instant t and a bifurcation parameter μ. The right hand side function f is called the evolution law of the dynamical system (Kutz *et al.*, 2016).

When this system has nonlinear characteristics, obtain its solution in a closed analytical form becomes a difficult task. In this sense, Koopman proposes a substitution of variables, expanding the number of observable states to encompass nonlinearities as components of the state space itself (Mezić, 2013; Mezić, 2005).

Through this modification, it is possible to describe the system with a linear dynamics that takes one current state to the next through a simplified operator, the Koopman operator $\mathcal{K}$. The discrete representation of this formulation is described as

$$g(\boldsymbol{x}_{k+1}) = \mathcal{K}\ (g(\boldsymbol{x}_k))\ , \tag{2.2}$$

where g represents this imposed change of variables and k represents a discrete instant of time.

The downside of this technique is the possibility of facing a closure problem that takes the system of finite dimensions to a system of infinite dimension (Budišić; Mohr; Mezić, 2012).

2.2. STATE-SPACE EXPANSION

Two examples for the state-space expansion are presented in this section, the first when a finite dimension is enough to make the system linear, while in the second, an infinite-dimensional expansion is required.

2.2.1 Polynomial Nonlinearity

Suppose a certain dynamical system has its evolution law defined by the following system of ordinary differential equations

$$\begin{cases} \dot{x}_1 = a x_1 \\ \dot{x}_2 = b\, x_1^n + c\, x_2\,, \end{cases} \tag{2.3}$$

which is a nonlinear system, with a polynomial nonlinearity.

Accordingly with the Koopman theory, it is possible to reach an equivalent linear system through an expansion of the state space. Thus, we chose the convenient change of variables:

$$\begin{aligned} y_1 &= x_1 \\ y_2 &= x_1^n \\ y_3 &= x_2\,. \end{aligned} \tag{2.4}$$

To match the pattern shown in the Eq. (2.2), it is necessary to compute the new variable's derivatives:

$$\begin{aligned} \dot{y}_1 &= \dot{x}_1 = a\, x_1 = a\, y_1 \\ \dot{y}_2 &= n\, x_1^{n-1}\, \dot{x}_1 = n x_1^{n-1}(a\, x_1) = n\, a\, x_1^n = n\, a\, y_2 \\ \dot{y}_3 &= \dot{x}_2 = b\, x_1^n + c\, x_2 = b\, y_2 + c\, y_3 \end{aligned}$$

So, we reach a new state space representation, with one more variable, but converted into a linear system of ordinary differential equations:

$$\begin{bmatrix} \dot{y}_1 \\ \dot{y}_2 \\ \dot{y}_3 \end{bmatrix} = \begin{bmatrix} a & 0 & 0 \\ 0 & n\,a & 0 \\ 0 & b & c \end{bmatrix} \begin{bmatrix} y_1 \\ y_2 \\ y_3 \end{bmatrix}$$

2.2.2 Simple Pendulum

Although a naive physical example, the simple pendulum provides a powerful insight into how some systems require an infinite expansion of the dimensional state space to make the system linear. To achieve this understanding, we begin with the characteristic equation of its simplest configuration, with no damping or external force, given by

$$\ddot{\theta} = -\frac{g}{L}\sin\theta\,, \tag{2.5}$$

where θ is the angle between the pendulum and the vertical, g is the gravity acceleration, and L is the string length. Just in order to simplify the approach take $k = -\frac{g}{L}$.

$$\ddot{\theta} = k\sin\theta \tag{2.6}$$

$$\begin{aligned} x_1 &= \dot{\theta} & x_4 &= \sin\theta\cos\theta \\ x_2 &= \sin\theta & x_5 &= \dot{\theta}^2\sin\theta \\ x_3 &= \dot{\theta}\cos\theta & &\vdots \end{aligned} \tag{2.7}$$

Again, it is necessary to compute the new variable's derivatives to match the pattern of the Eq. (2.2):

$$\begin{aligned} \dot{x}_1 &= \ddot{\theta} = k\sin\theta = kx_2 \\ \dot{x}_2 &= \dot{\theta}\cos\theta = x_3 \\ \dot{x}_3 &= \ddot{\theta}\cos\theta - \dot{\theta}\dot{\theta}\sin\theta = k\sin\theta\cos\theta - \dot{\theta}^2\sin\theta = \dot{x}_3 = kx_4 - x_5 \\ \dot{x}_4 &= \dot{\theta}\cos^2\theta - \dot{\theta}\sin^2\theta = \dot{\theta}(1 - \sin^2\theta - \sin^2\theta) = \dot{\theta} - 2\dot{\theta}\sin^2\theta = x_1 - x_6 \\ \dot{x}_5 &= 2\dot{\theta}\ddot{\theta} - \dot{\theta}^3\cos\theta = 2\dot{\theta}(k\sin\theta) - \dot{\theta}^3\cos\theta = 2k\dot{\theta}\sin\theta - \dot{\theta}^3\cos\theta \\ &\vdots \end{aligned}$$

Notice that in the simple pendulum case, the underlying sinusoidal nonlinearity leads to a state space that can not close itself, so an infinite dimensional system emerges. Considering that the simple pendulum is a example with a sinusoidal response, also common for a broad of applications, the infinite dimensional problem can be frequently achieved.

3 DINAMIC MODE DECOMPOSITION

This chapter delves into the up-and-coming technique called dynamic mode decomposition (DMD) used to approximate the Koopman operator in the context of data-driven science and engineering. The Section 3.1 describe the theoretical foundations of the theory, while the Section 3.2 enters a more practical field, describing the algorithm development.

3.1. THEORETICAL FOUNDATIONS

Dynamic mode decomposition is a method that uses observation data from a dynamical system to perform a spatio-temporal decomposition of its state representation through the combination of order reduction methods and dynamic mode analysis (Kutz *et al.*, 2016; Kutz; Proctor; Brunton, 2018).

In this formalism, the original nonlinear dynamical system in Eq. 2.1 is approximated by a linear proxy

$$\frac{d}{dt}\boldsymbol{x}(t) = \boldsymbol{\mathcal{A}}\,\boldsymbol{x}(t)\,, \tag{3.1}$$

in which the matrix $\boldsymbol{\mathcal{A}} \in \mathbb{R}^{M\times M}$ represents the linear Koopman operator in a suitable basis and is analogous to the dynamic matrix seen in mechanical systems like vibrating beams and rods. Employing an eigendecomposition of matrix $\boldsymbol{\mathcal{A}}$, i.e, $\boldsymbol{\mathcal{A}}\,\boldsymbol{\phi}_k = \omega_k\,\boldsymbol{\phi}_k$, it is possible to write the novel state vector as

$$\boldsymbol{x}(t) = \sum_{k=1}^{M} \boldsymbol{\phi}_k\, e^{(\omega_k\, t)}\, b_k\,, \tag{3.2}$$

where $\boldsymbol{\phi}_k \in \mathbb{R}^M$ are eigenvectors of $\boldsymbol{\mathcal{A}}$, ω_k the corresponding eigenvalues, and b_k are the initial condition coordinates in the eigenvector basis, which reads as

$$\boldsymbol{x}(t) = \boldsymbol{\Phi}\, e^{(\boldsymbol{\Omega}\, t)}\, \boldsymbol{b}\,, \tag{3.3}$$

where the matrix $\boldsymbol{\Phi} \in \mathbb{R}^{M\times M}$ collects the eigenvectors $\boldsymbol{\phi}_k$ on its columns, $\boldsymbol{\Omega} \in \mathbb{R}^{M\times M}$ is a diagonal matrix with the corresponding eigenvalues, and $\boldsymbol{b} \in \mathbb{R}^M$ collects the coordinates b_k.

Once the continuous dynamical system is defined as in Eq. (3.1), its discrete-time analog is given by

$$\boldsymbol{x}_{k+1} = \boldsymbol{A}\,\boldsymbol{x}_k\ , \tag{3.4}$$

where the state vector $\boldsymbol{x}_k \in \mathbb{R}^M$ here is defined for discrete-time instants $t_k = k\,\Delta t$, for $k = 1, \cdots N$. Therefore, this novel matrix $\boldsymbol{A}$ is defined in terms of the original matrix $\mathcal{A}$ via matrix exponentiation

$$\boldsymbol{A} = e^{(\mathcal{A}\,\Delta t)}\,, \tag{3.5}$$

and the solution for the discrete system is

$$\boldsymbol{x}_k = \sum_{j=1}^{r} \boldsymbol{\phi}_j\,\lambda_j^k\,b_j = \boldsymbol{\Phi}\,\boldsymbol{\Lambda}^k\,\boldsymbol{b}\,, \tag{3.6}$$

where λ_j are the eigenvalues whenever $\boldsymbol{\phi}_j$ are the eigenvectors of $\boldsymbol{A}$.

The DMD obtains the best fit for $\boldsymbol{y}_k$ in a way that

$$\boldsymbol{X'} \approx \boldsymbol{A}\boldsymbol{X}\,, \tag{3.7}$$

where

$$\boldsymbol{X} = \begin{bmatrix} | & & | \\ \boldsymbol{x}_1 & \cdots & \boldsymbol{x}_{N-1} \\ | & & | \end{bmatrix} \qquad \text{and} \qquad \boldsymbol{X'} = \begin{bmatrix} | & & | \\ \boldsymbol{x}_2 & \cdots & \boldsymbol{x}_{N} \\ | & & | \end{bmatrix}\,, \tag{3.8}$$

are matrices in $\mathbb{R}^{M\times(N-1)}$ that organize the available data in chronological order. Both $\boldsymbol{X}$ and $\boldsymbol{X'}$ contain state data in their rows and time instants in their columns. The difference between $\boldsymbol{X}$ and $\boldsymbol{X'}$ is that insofar $\boldsymbol{X}$ contains data from the first instant to the second to last, and the $\boldsymbol{X'}$ is composed of its version shifted one time instant, namely from second instant to last instant.

In a more formal context, this approximation problem is stated as a regression problem in a matrix space given by

$$\arg\min_{\boldsymbol{A}} ||\boldsymbol{X'} - \boldsymbol{A}\boldsymbol{X}||_F\,, \tag{3.9}$$

in which $||.||_F$ is the Frobenius norm

$$||\boldsymbol{X}||_F = \sqrt{\sum_{j=1}^{M}\sum_{k=1}^{N} X_{jk}^2}\,. \tag{3.10}$$

The solution for this regression problem can be obtained by using the Moore-Penrose pseudoinverse of $\boldsymbol{X}$, called $\boldsymbol{X}^\dagger$. Coming out of the $\boldsymbol{A}$ matrix, the solution for the discrete-time system is directly taken from the Eq. (3.6), so that

$$\boldsymbol{A} = \boldsymbol{X'}\boldsymbol{X}^\dagger\,. \tag{3.11}$$

A challenge for this approach is that the computation of the pseudo-inverse from large data matrices is a costly process. Toward dealing with this dare a truncation step is applied in the algorithm (Kutz *et al.*, 2016).

3.2. ALGORITHM DESCRIPTION

The process of DMD as applied to the analysis of complex systems is depicted in Fig. 3. The procedure begins with the pre-processing stage where snapshots of the system are taken at sequential time intervals $t_1, t_2, \cdots, t_N$. These snapshots are then organized into two matrices, $\boldsymbol{X}$ and $\boldsymbol{X}'$, representing consecutive states. Following pre-processing, the DMD algorithm is applied to these matrices to compute the matrix $\boldsymbol{A}$ which approximates the best-fit linear operator that maps between the states. This involves the computation of singular value decomposition (SVD) as explained by Golub e Loan (2013), and the subsequent DMD modes and eigenvalues. In the diagnosis phase, the eigenvalues λ and modes $\boldsymbol{\Phi}$ are extracted, revealing the intrinsic frequencies and spatial structures governing the system dynamics. Lastly, the system's future states are predicted by extrapolating the dynamic modes forward in time, allowing both the reconstruction of the system at known time points and the prediction of future states.

The DMD algorithm is elucidated through the following steps:

1. **Pre-processing:**

   - *Data Organization:* Assemble the state snapshot matrices into a composite data matrix. Each column encapsulates the complete state information at a respective time step.
   - *Matrix Partition:* Divide the assembled data matrix into two matrices, $\boldsymbol{X}$, and $\boldsymbol{X}'$. Matrix $\boldsymbol{X}$ contains columns from the first to the penultimate time step, while $\boldsymbol{X}'$ includes columns from the second to the final time step.

2. **DMD factorization:**

   - *Economy SVD:* Perform the economy Singular Value Decomposition (SVD) of $\boldsymbol{X}$, to discern the principal modes of the system:

$$\boldsymbol{X} = \boldsymbol{U}\,\boldsymbol{\Sigma}\,\boldsymbol{V}^T$$

for which $\boldsymbol{U} \in \mathbb{R}^{M\times R}$ and $\boldsymbol{V} \in \mathbb{R}^{(N-1)\times R}$ are orthogonal matrices , and $\boldsymbol{\Sigma} \in \mathbb{R}^{R\times R}$ is a diagonal matrix, and R is the rank of $\boldsymbol{X}$.

- *Matrix Truncation:* Approximate $\boldsymbol{X}$ with a truncated set of matrices capturing the dominant features of the decomposition:

$$\boldsymbol{X} \approx \boldsymbol{U}_r\, \boldsymbol{\Sigma}_r\, \boldsymbol{V}_r^T$$

where $\boldsymbol{U}_r = \boldsymbol{U}(:, 1:r)$, $\boldsymbol{V}_r = \boldsymbol{V}(:, 1:r)$, and $\boldsymbol{\Sigma}_r = \boldsymbol{\Sigma}(1:r, 1:r)$, where the reduction order r is such that $r \ll R$.

- *POD Projection:* Utilize Proper Orthogonal Decomposition (POD) to project the matrix $\boldsymbol{A}$ onto a reduced-order space:

$$\tilde{\boldsymbol{A}} = \boldsymbol{U}_r^T\, \boldsymbol{A}\, \boldsymbol{U}_r = \boldsymbol{U}_r^T\, \boldsymbol{X'}\, \boldsymbol{V}_r\, \boldsymbol{\Sigma}_r^{-1}$$

so that $\tilde{\boldsymbol{A}} \in \mathbb{R}^{r\times r}$.

- *Eigendecomposition:* Determine the eigenvalues and eigenvectors of the reduced matrix $\tilde{\boldsymbol{A}}$, which represent the dynamics of the reduced system:

$$\tilde{\boldsymbol{A}}\, \boldsymbol{W} = \boldsymbol{W}\, \boldsymbol{\Lambda}$$

where $\boldsymbol{W} \in \mathbb{R}^{r\times r}$ collects in its columns the eigenvectos of $\tilde{\boldsymbol{A}}$, $\boldsymbol{\phi}_k$, and $\boldsymbol{\Lambda} \in \mathbb{R}^{r\times r}$ is a diagonal matrix with the associated eigenvalues λ_k.

3. **Dynamics Reconstruction:**

- *Eigendecomposition Mapping:* Map the eigendecomposition from $\tilde{\boldsymbol{A}}$ back to the full operator $\boldsymbol{A}$:

$$\boldsymbol{A} = \boldsymbol{\Phi}\, \boldsymbol{\Lambda}\, \boldsymbol{\Phi}^T$$

where the modal matrix $\boldsymbol{\Phi} \in \mathbb{R}^{M\times r}$ is such that $\boldsymbol{\Phi} = \boldsymbol{X'}\, \boldsymbol{V}_r\, \boldsymbol{\Sigma}_r^{-1}\, \boldsymbol{W}$.

- *Initial Value Problem (IVP):* Solve the IVP to reconstruct the dynamic state by means of modal expansion:

$$\boldsymbol{x}(t) \approx \boldsymbol{\Phi} \exp\left(\boldsymbol{\Omega}\, t\right) \boldsymbol{b}$$

where the elements of the diagonal matrix $\boldsymbol{\Omega}$ are such that $\omega_k = \ln \lambda_k / \Delta t$, and $\boldsymbol{b} = \boldsymbol{\Phi}^\dagger\, \boldsymbol{X}(:, 1)$.

4. **Post-processing:**

   - *Data Unpacking:* Convert the reconstructed data matrix, with its time instances represented as columns, back into the format of the original snapshot matrices.

The code below shows a pedagogical MATLAB implementation of this algorithm, where one of the steps described above is clearly indicated. The reader can download this code on GitHub (Araujo, 2024).

```
function [Phi, Omega, Xdmd, S] = dmd(X,dt,r)
    % Step 1: separate X e X' matrices
    X1 = X(:,1:end-1);  X2 = X(:,2:end);
    % Step 2: compute economy SVD
    [U,S,V] = svd(X1,'econ');
    %  Step 3: truncate main modes
    Ur = U(:,1:r); Sr = S(1:r,1:r); Vr = V(:,1:r);
    % Step 4: POD
    Atilde = Ur'*X2*Vr/Sr;
    % Step 5: Solve the eigen problem
    [W,Lambda] = eig(Atilde);
    % Step 6: Recover original eigenpairs
    Phi = X2*Vr/Sr*W;  Omega = log(diag(Lambda))/dt;
    % Step 7: Solve the IVP
    x0 = X1(:,1);  b = Phi\x0;
    snaps = size(X1,2);  t = (0:snaps-1)*dt;
    time_part = zeros(r,snaps);
    for n = 1:snaps
        time_part(:,n) = b.*exp(Omega*t(n));
    end
    Xdmd = Phi*time_part;
end
```

Figura 3 – Schematic overview of the DMD workflow. The top panel illustrates the pre-processing of system snapshots into data matrices. The middle panel outlines the DMD algorithm, including matrix construction and decomposition. The bottom left panel displays the frequencies and spatial modes resulting from the DMD diagnosis, while the bottom right panel shows both the reconstruction of past states and the prediction of future states using the identified dynamic modes. This multi-step process encapsulates the entire pipeline from data collection to predictive modeling in the application of DMD.

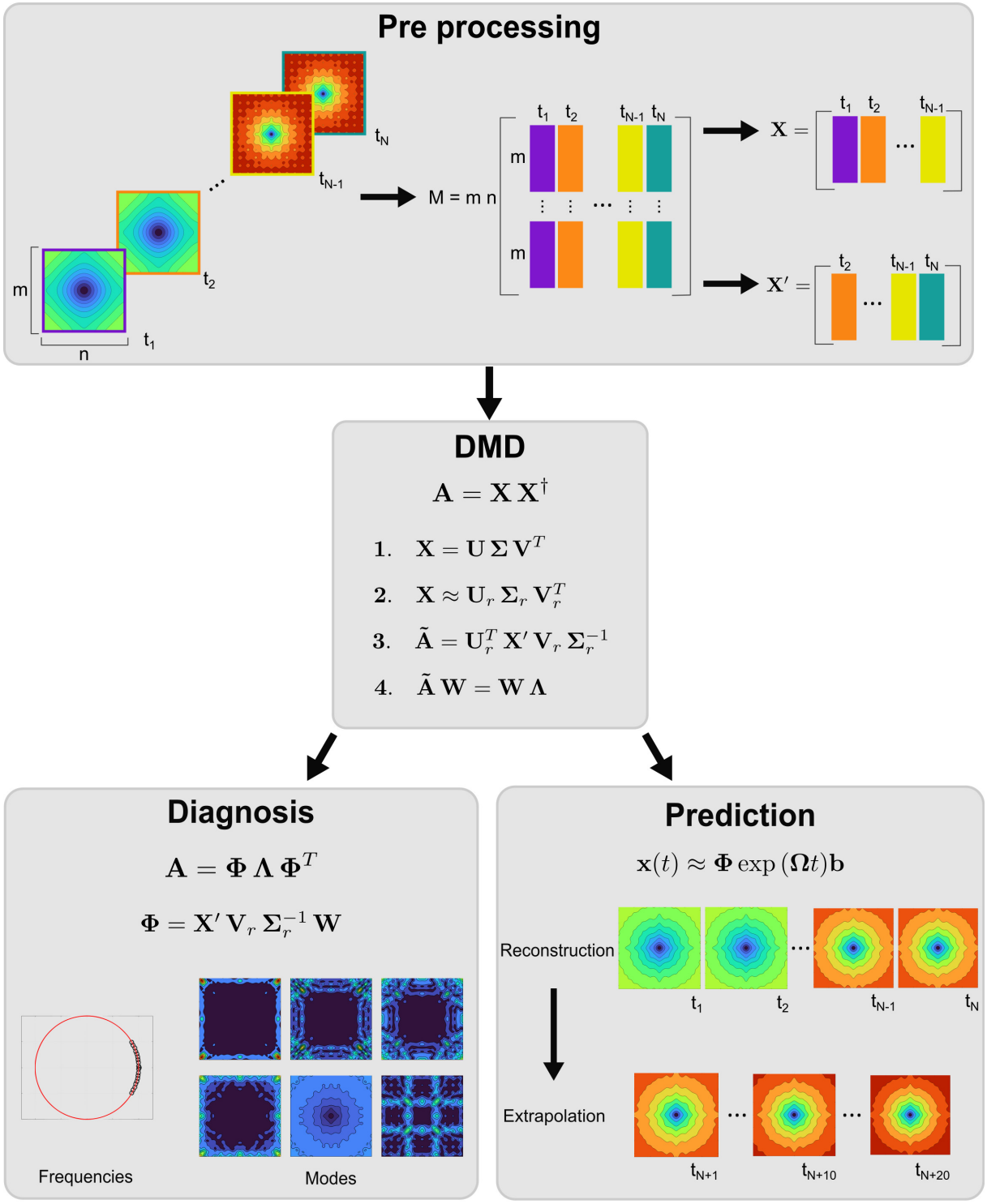

Source: Produced by the author.

4 RESULTS AND DISCUSSION

This chapter overviews the results from the applied metodology, concerning the field generation, the modal decomposition, the field reconstruction, and an exploration of how truncation influences into the quality of the outcome. Hence, the chapter is organized in four sections, namely: Section 4.2, showcases three ways employed to generate data as an input for the DMD algorithm; Section 4.2, presenting the singular values for the fields and the truncation taken; Section 4.3, which covers the modal decomposition; Section 4.4, providing a visual comparison between the original and reconstructed fields; and finally the Section 4.5, which discusses the similarity for different truncation values.

4.1. DATA GENERATION

This section presents three ways used to generate data for the DMD algorithm application, so it is composed of three subsections: the generation using optimization benchmark functions, in subsection 4.1.1; athwart the analytical solution for a heat diffusion problem, in subsection 4.1.2; and finally through the sensoring of a heat diffusion experiment, in subsection 4.1.3.

4.1.1 Mathematical fields

Aiming to illustrate the ability of dynamic mode decomposition in reconstructing spatio-temporal patterns from data, four nonlinear functions are considered as benchmarks here, namely Ackley, Rastrigin, Griewank, and Schaffer N.2 functions. All of them are typically used to evaluate the performance of optimization algorithms due to their complexity and several optimal values (Spall, 2003), an interesting feature in the context of challenging the DMD capability. The Tab. 1 shows the expressions for these functions such as their usual domains considered for evaluation.

For sake of computation, the space coordinates are discretized with the aid of a 1000×1000 regular grid, which results in the static fields represented in the Fig. 4.

In order to incorporate temporal dynamics into our analysis, we introduce a time-dependent variation into the spatial coordinates. The position x_i is redefined as a function of time according to a harmonic signal, i.e.,

Tabela 1 – Functions used as benchmark for optimization problems with their usual domains description.

Name	**Function**	**Domain**
Ackley	$f_a = -20\,\exp\left(-0.2\sqrt{0.5\sum_{i=1}^{2} x_i^2}\right) - \exp\left(0.5\sum_{i=1}^{2}\cos\left(2\pi x_i\right)\right) + 20 + e$	$x_i \in [-32.768, 32.768]$
Rastrigin	$f_r = 20 + \sum_{i=1}^{2}\left(x_i^2 - 10\cos\left(2\pi x_i\right)\right)$	$x_i \in [-5.12, 5.12]$
Griewank	$f_g = \sum_{i=1}^{2}\frac{x_i^2}{4000} - \prod_{i=1}^{2}\cos\left(\frac{x_i}{\sqrt{i}}\right) + 1$	$x_i \in [-600, 600]$
Schaffer N. 2	$f_s = 0.5 + \frac{\sin^2\left(x_1^2 - x_2^2\right) - 0.5}{\left(1 + 0.001(x_1^2 + x_2^2)\right)^2}$	$x_i \in [-50, 50]$

Source: Produced by the author.

$$x_i(t) = A\,\sin\left(t\right), \tag{4.1}$$

where A represents the amplitude, corresponding to the magnitude of the original static coordinate x_i. The function is designed to oscillate with time, bounded within the interval $0 \leq t < \pi/4$. To discretize the temporal domain for our simulations, we divide the time interval into 100 equidistant points.

Applying these modifications to the benchmark functions, the dynamical fields are shown in Fig. 5. The three columns correspond to three different snapshots of the field, in the 1-st, 50-th and 100-th instants, the first row is the evolution of Ackley function, the second one of Rastrigin, the third is the Griewank instants, and the fourth is relative to the Schaffer N.2. Aiming to emulate disturbs in the measurements as well as uncertainties, white Gaussian noise was added to the dynamical fields with amplitude equivalent to 10% of the total amplitude of the field, reaching the instants presented in the Fig. 6.

Figura 4 – Static field of the (a) Ackley, (b) Rastrigin, (c) Griewank, (d) Schaffer N.2 functions, commonly used for optimization problem benchmark.

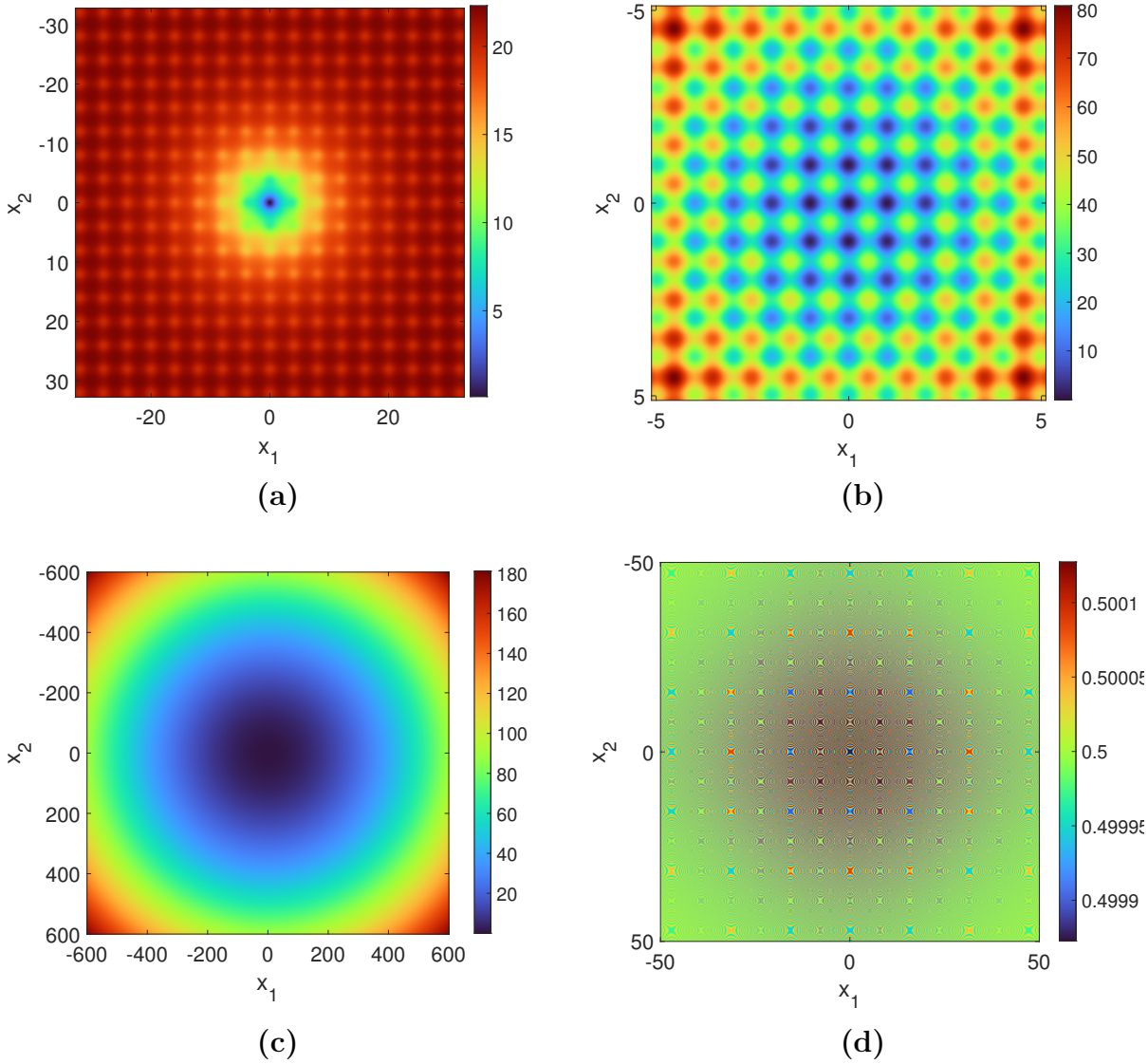

Source: Produced by the author.

Figura 5 – Dynamical field evolution of (a) Ackley, (b) Rastrigin, (c) Griewank, (d) Schaffer N.2 functions. Three columns are presented corresponding to three time instants for each field: 1^{st} in the left, 50^{th} in the middle, 100^{th} in the right.

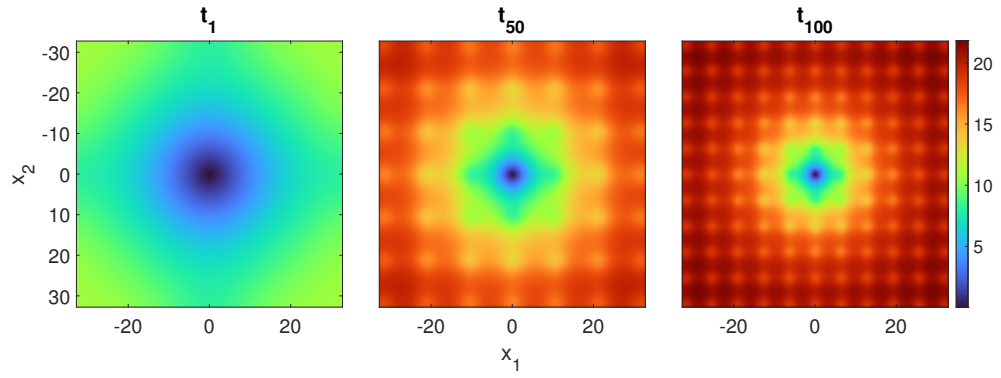

(a)

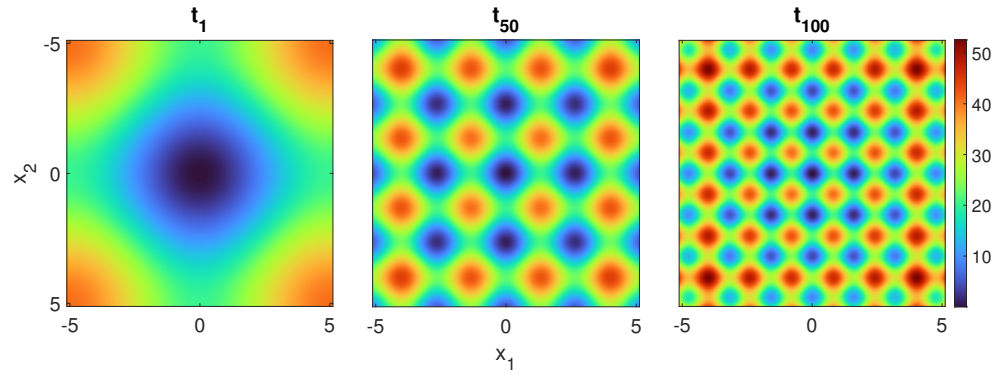

(b)

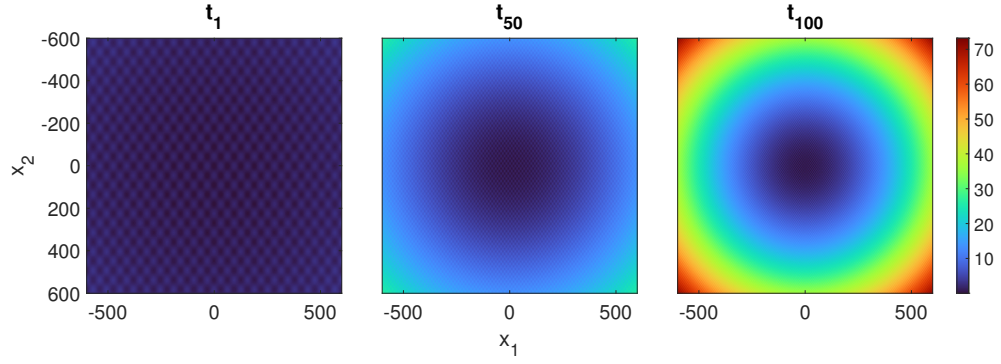

(c)

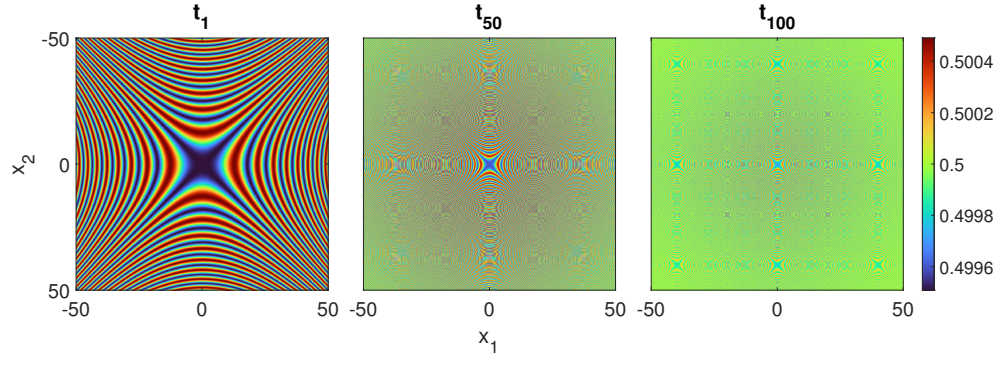

(d)

Source: Produced by the author.

Figura 6 – Gaussian noise added version (10%) of the dynamical field evolution of (a) Ackley, (b) Rastrigin, (c) Griewank, (d) Schaffer N.2 functions. Three columns are presented corresponding to three time instants for each field: 1^{st} in the left, 50^{th} in the middle, 100^{th} in the right.

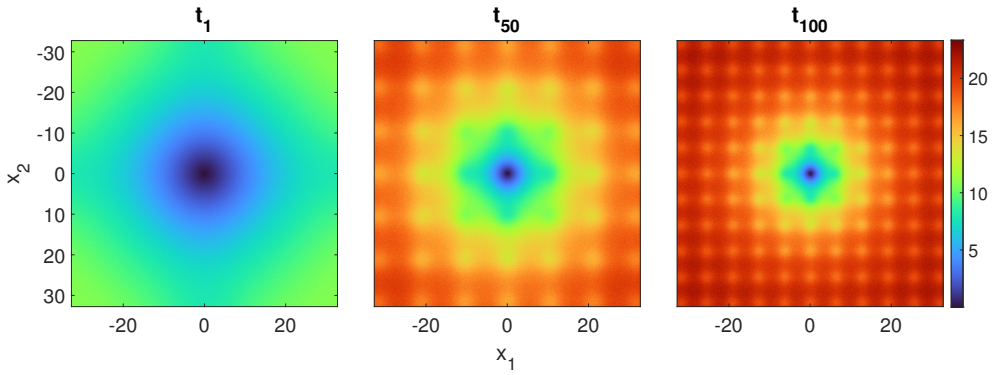

(a)

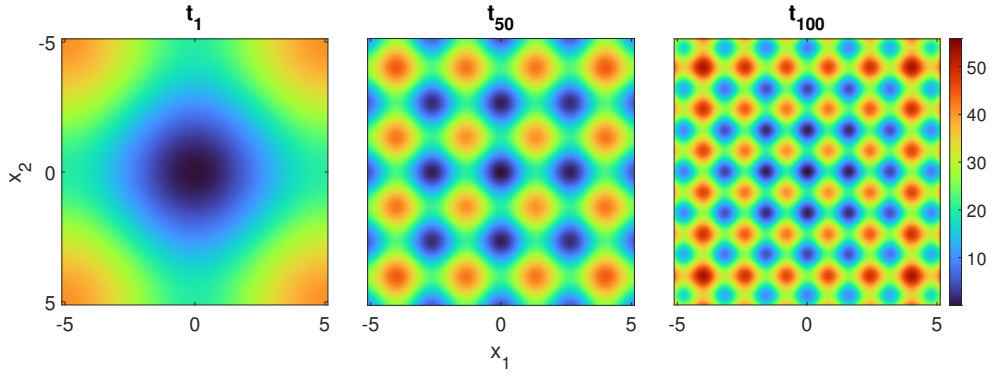

(b)

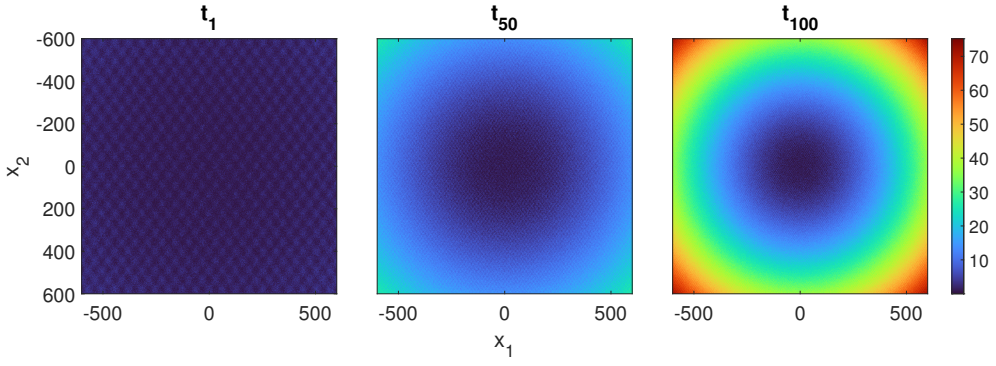

(c)

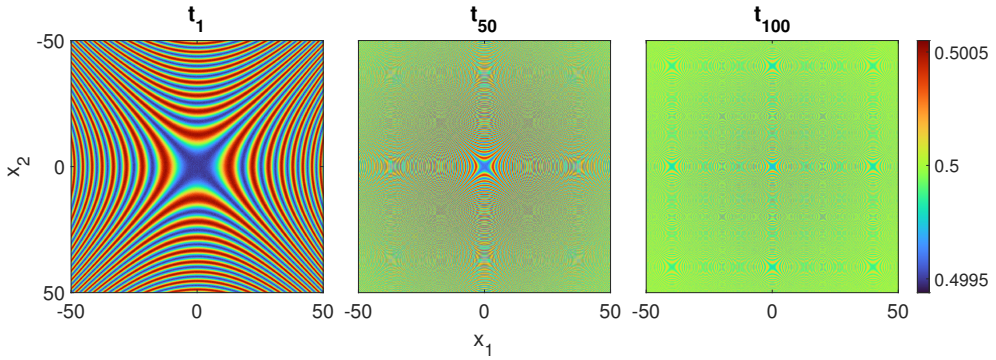

(d)

Source: Produced by the author.

4.1.2 Heat diffusion field

Going to a physical scenario, the DMD is then applied to a temperature dynamical field. The situation proposed is a plate of isotropic and homogeneous material cooling. From (Lienhard V; Lienhard IV, 2024) the heat transfer formulation for the conduction mechanism, when the conductivity is considered constant and the material is incompressible, is given by

$$\nabla^2 T + \frac{\dot{q}}{K} = \frac{1}{\alpha}\frac{\partial T}{\partial t} \tag{4.2}$$

with T being the temperature, $\dot{q}$ the heat flux from the thermal source, K the thermal conductivity, α the thermal diffusivity, ρ the density, $c = c_v = c_p$ the specific heat, and t the time. Simplifying the equation for a situation with no thermal source and thermal diffusivity unitary ($\alpha = 1$), the Eq. 4.2 is subsumed to

$$\nabla^2 T = \frac{\partial T}{\partial t} \quad . \tag{4.3}$$

The boundary conditions proposed to evaluate the temperature field $T(\mathbf{x}, t)$ in the domain $\mathbf{x} = (x, y)$ with $x \in [0, 1]$, and $y \in [0, 1]$ are:

$$\begin{cases} T(0, y, t) = T(1, y, t) = 0 \\ T(x, 0, t) = T(x, 1, t) = 0 \end{cases} \tag{4.4}$$

while the initial condition is given by $T(x, y, 0) = 1$. Thus, accordingly to (Sampaio; Wolter, 2001) the solution for the Eq. 4.3 becomes

$$T(x, y, t) = \sum_i \sum_j \frac{4}{ij\pi^2} \left(1 - \cos\left(i\pi\right)\right) \left(1 - \cos\left(i\pi\right)\right) e^{-(i^2+j^2)\pi^2 t} \sin\left(i\pi x\right) \sin\left(j\pi y\right) \quad . \tag{4.5}$$

Evaluating this solution in the proposed domain for 100 time instants, the resulting dynamical field is displayed in the Fig. 7, also with three time instants ($1^s t$, 20^{th}, and 50^{th}) to show up the time evolution.

Figura 7 – Analytical temperature field evolution of a cooling plate through conduction. Three columns are presented corresponding to three time instants for each field: 1^{st} in the left, 20^{th} in the middle, 50^{th} in the right.

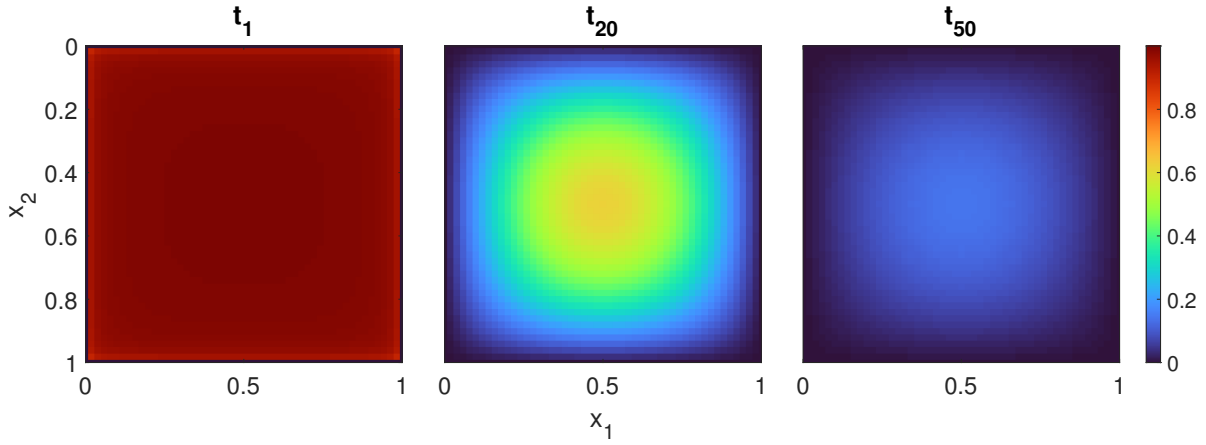

Source: Produced by the author.

Toward considering a situation closer to an experimental, when the sensing is limited in resolution, a coarser sampling in the space is assumed, by taking just a 10×10 mesh grid, presented in the Fig. 8. Again, to emulate the disturbs and uncertainties, Gaussian white noise is added to the field, with intensity equivalent to 10% of the overall amplitude of the original field, exposed in the Fig. 9.

Figura 8 – Analytical temperature field evolution of a cooling plate through conduction. Three columns are presented corresponding to three time instants for each field: 1^{st} in the left, 20^{th} in the middle, 50^{th} in the right.

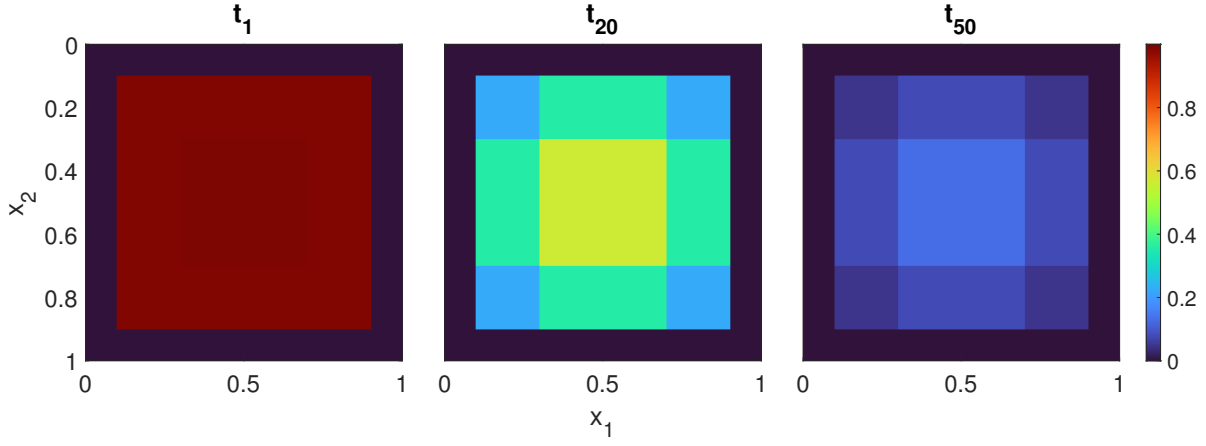

Source: Produced by the author.

Figura 9 – Analytical temperature field evolution of a cooling plate through conduction. Three columns are presented corresponding to three time instants for each field: 1^{st} in the left, 20^{th} in the middle, 50^{th} in the right.

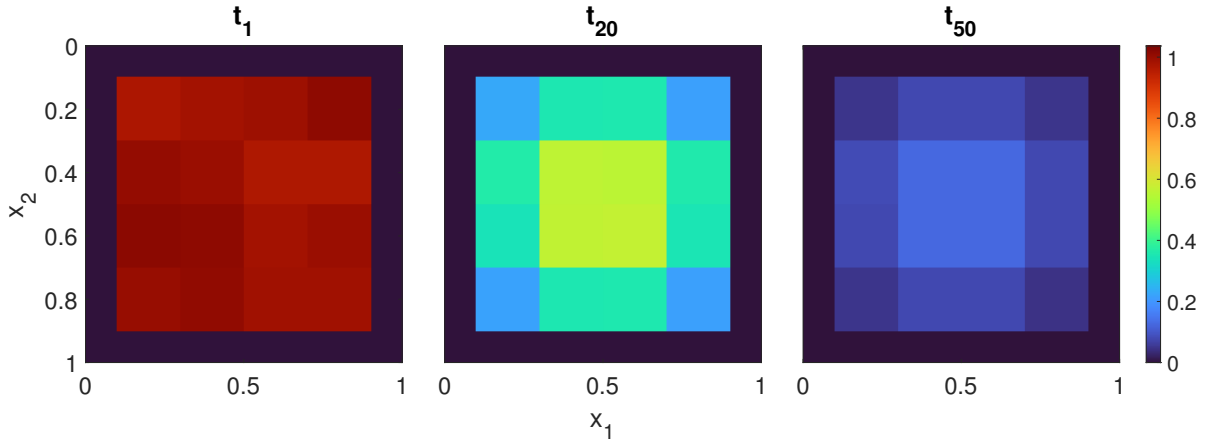

Source: Produced by the author.

4.1.3 Experimental field

Progressing to a more realistic scenario, an experiment was designed to generate a dynamical temperature field as input for the DMD algorithm. The experimental configuration is illustrated in Fig. 10, with two perspectives provided to highlight the arrangement of components. The primary objective of this experiment was to observe and analyze the temperature evolution of an aluminum plate subjected to a controlled heat source, represented by a heat gun. The materials used was:

- Aluminum Plate: Dimensions of 305 mm × 250 mm × 1.5 mm;
- Heat Gun: Model Hikari HK-508, rated at 1500W;
- Thermal Imager: Fluke Ti25, used to capture the temperature field;
- Component Supports: Used to align the heat gun and thermal imager at specific positions.

To ensure accurate temperature measurements, the aluminum plate was painted black. This was necessary to correct for the low emissivity and high reflectivity of the aluminum surface, which would otherwise lead to inaccurate thermal readings from the imager.

The experimental procedure consisted of two stages: a heating phase followed by a cooling phase consisting of:

1. **Heating Phase:**
    - The heat gun was directed at the center of the aluminum plate and turned on for 150 seconds;
    - During this phase, the plate's surface temperature gradually increased, forming a dynamic temperature field.
2. **Cooling Phase:**
    - After the heat gun was turned off, the plate was left to cool naturally for 300 seconds.
    - No external cooling mechanism was used, allowing the plate to return to ambient temperature through natural convection and radiation.

Throughout both stages, temperature data were collected using the Fluke Ti25 thermal imager, with frames captured every 10 seconds. This resulted in a total of 44 frames: 15 during the heating phase (0–150 seconds) and 30 during the cooling phase (150–450 seconds). These frames provided a time-resolved dataset of the temperature distribution across the plate's surface, serving as input for the DMD algorithm to analyze the underlying spatial and temporal dynamics.

Three frames are stated in the Fig. 11, that correspond to 1^{st}, 15^{th}, and 30^{th} instants (0 s, 150 s, and 300 s), outlining the visualization of the normalized temperature field evolution. It's important to highlight that the output from the thermal imager is given in a three-layer matrix for each frame, the RGB (red, green, blue) representation of colors. Therefore, the DMD must also to be performed in three channels, each one with its own truncation choice.

Figura 10 – Experimental setup for measuring the temperature field evolution of a aluminum plate under a heat gun as a heat source. Two perspectives are shown, a front view (a) and a back view (b).

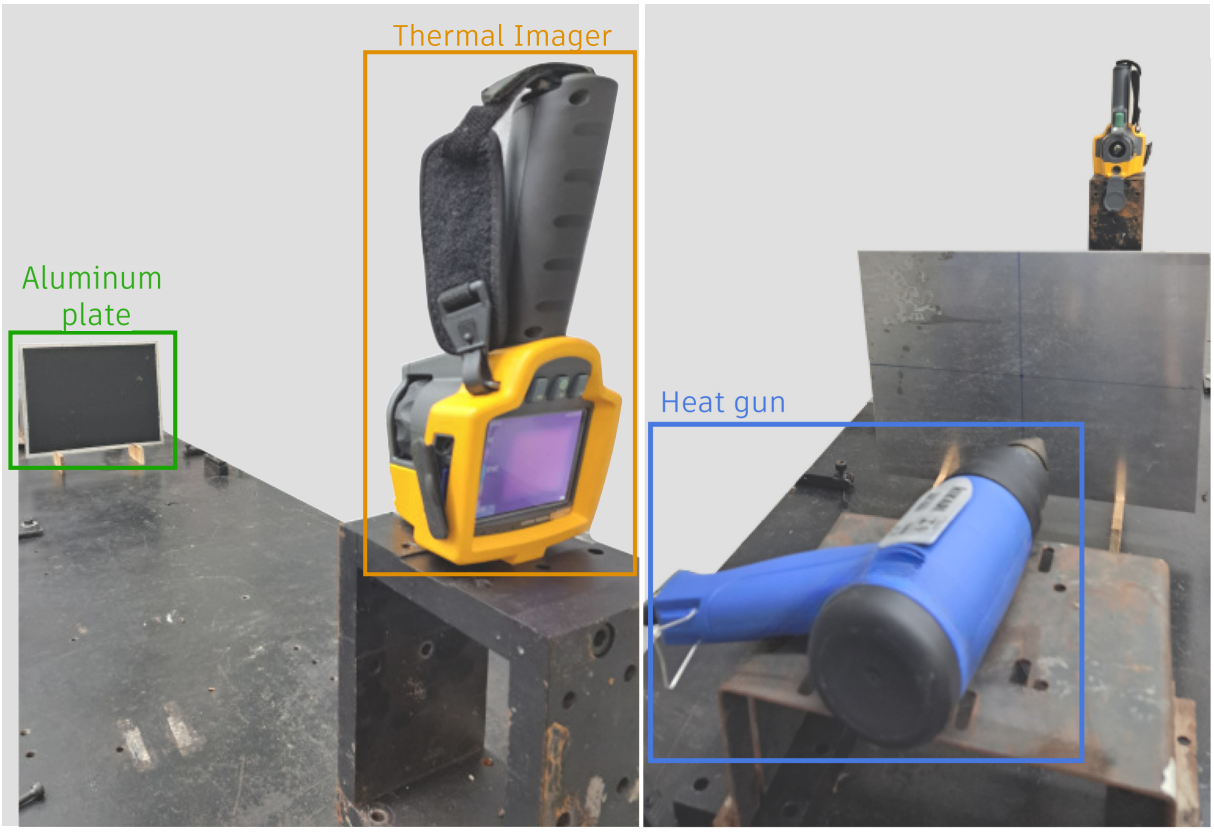

Source: Produced by the author.

Figura 11 – Experimental temperature field evolution of a aluminum plate under a heat gun source. Three columns are presented corresponding to three time instants for each field: 1^{st} in the left, 15^{th} in the middle, 30^{th} in the right.

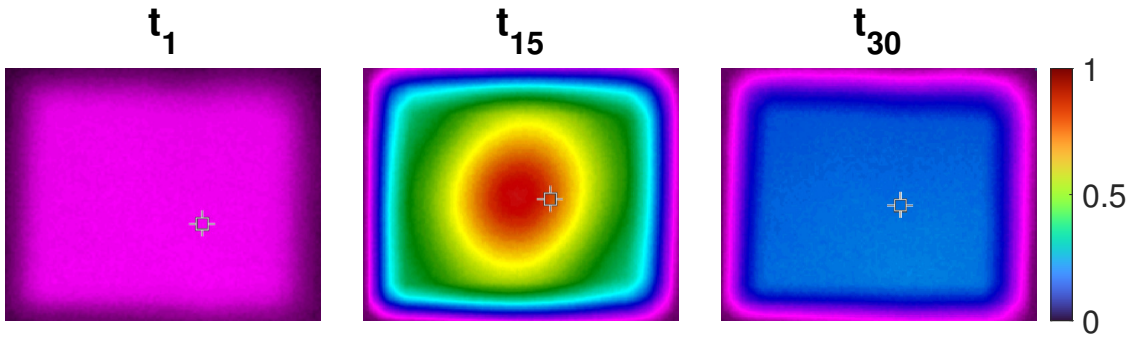

Source: Produced by the author.

4.2. SINGULAR VALUES

First of all, the singular values of $\boldsymbol{X}$ are the first step to achieve de modal decomposition of data and must be examined to provide insights into truncation taken into the algorithm. The process of obtaining the singular values is described as the first step of the DMD factorization in the Section 3.2, and computed in the sixth row of the simplified code presented in that section.

The singular values for the analytical dynamical fields are presented in the Figure 12, while for the experimental fields are in the Fig. 13. Their magnitudes are in the log scale into the vertical axis, and the first 15 indexes of singular values are in the horizontal axis. The region containing just main contributions is highlighted in light gray and will be the only singular values taken in the truncation.

Notice that for the Ackley function, despite the first nine singular values being considerably bigger than the next ones, there is a second baseline of values with similar importance. Therefore, using nine modes yields a better reconstruction, which is confirmed in the further truncation analysis. Similarly, for the Rastrigin function, despite the first singular value is also larger than the others, truncating with seven modes is the option chosen to encompass the next level of singular values.

Griewank function, in its turn, has two modes remarkably dominant, the same for the Schaffer N.2 which needs only one singular value, and the Heat diffusion field also with two modes.

As the experimental field has three layers of information for the red, green, and blue shades, there are also three singular values decomposition. Spot that both of them have a more subtle decay, such that more singular values are needed for a good description of the field evolution. For the red channel, singular values seems stabilize in a small level after the 21^{th} mode, so that 21 modes are chosen. Following the same criteria, for the green and blue channels 18 modes are selected.

4.3. MODES AND FREQUENCIES

In DMD, modes represent the dominant spatial patterns in a system's evolution, with each mode associated with a complex eigenvalue that dictates its temporal behavior — whether it oscillates, grows, or decays. Frequencies within the unit circle indicate

Figura 12 – Singular values of $\boldsymbol{X}$ matrix for the datasets corresponding to the spatio-temporal patterns of the Ackley (a), Rastrigin (b), Griewank (c), Schaffer N.2 (d) functions, and for the heat diffusion field (e).

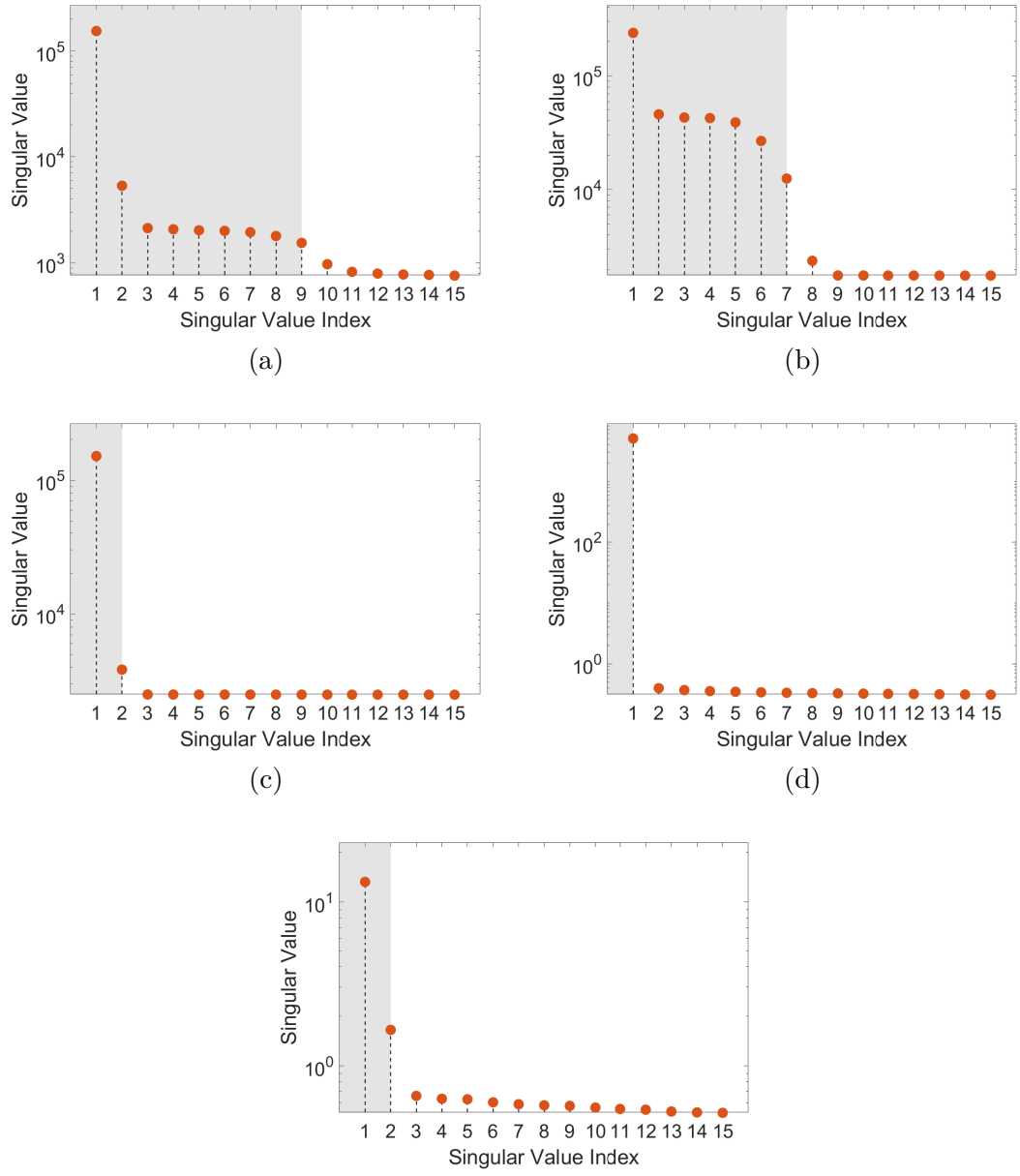

Source: Produced by the author.

stability, while those outside it signal instability (Strogatz, 2014). These modes help uncover key dynamics, such as vortex patterns in fluid flows or deformation shapes in structures, and their amplitudes reflect their contribution to the system's behavior. By focusing on the most relevant modes, DMD provides a low-dimensional representation that captures essential dynamics.

From the nine modes taken in the Ackley field decomposition, six are shown in

Figura 13 – Singular values of $\boldsymbol{X}$ matrix for the datasets corresponding to the spatio-temporal patterns of the experimental components field red (a), green (b), blue (c).

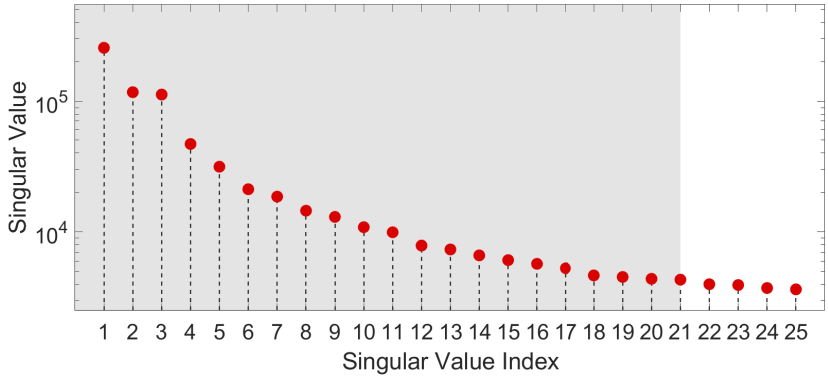

(a)

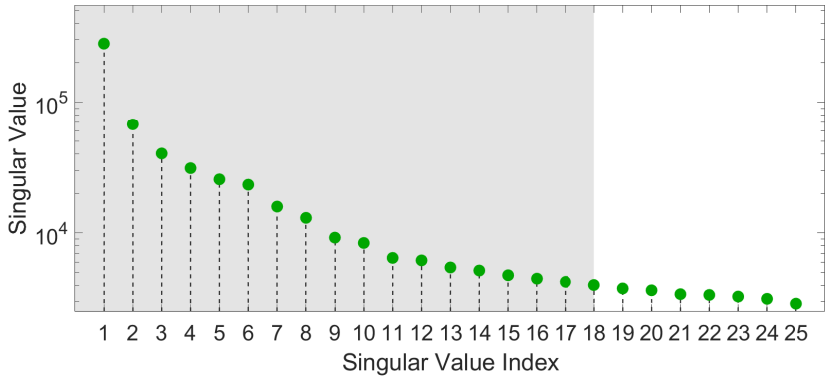

(b)

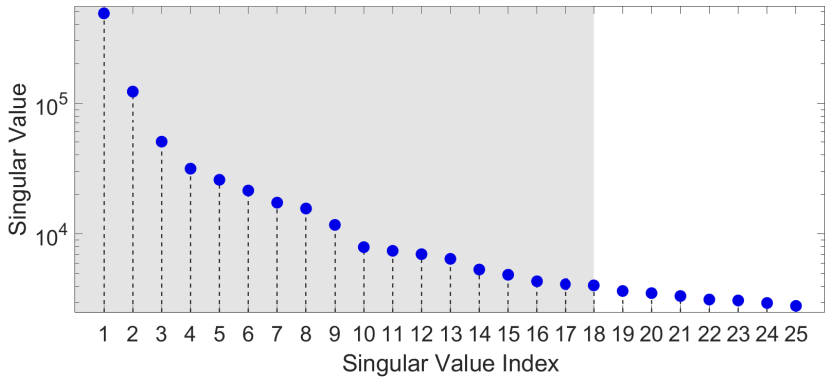

(c)

Source: Produced by the author.

the Fig. 14. The first and second modes are very similar, with a slight difference of the third one, which also compose a pair of close modes with the fourth mode, the reason why fourth is omitted. The same happens with the fifth and sixth modes, and with the pair eight and nine. The first four modes recover mainly the global surface, while the next ones resume the local oscillations with their local minima.

Figura 14 – Modes and frequencies for Ackley decomposition

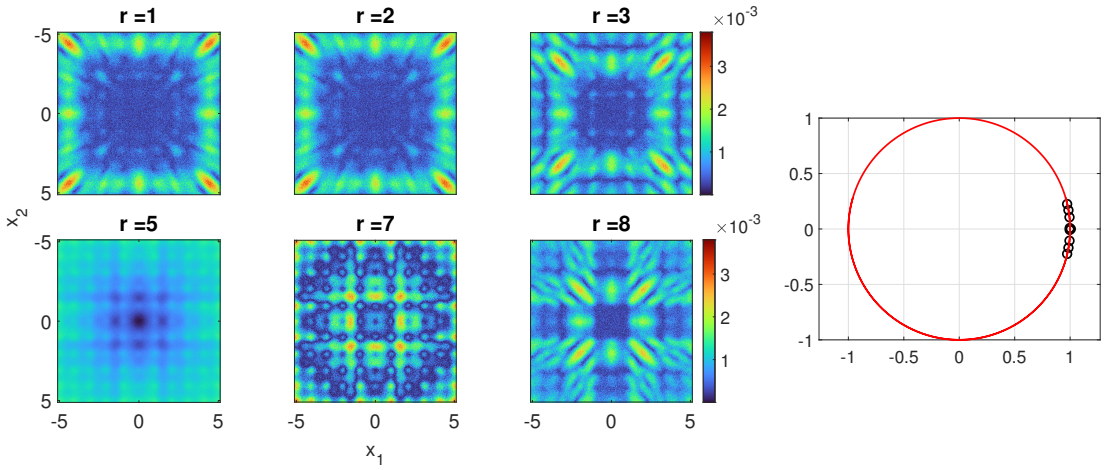

Source: Produced by the author.

Respecting the Rastrigin field, an alike approach is taken. Six modes are presented in the Fig. 15, the first and second are very similar, as like as third and fourth, and sixth and seventh pairs. Recurrently, the first modes are responsible for the major information about the field evolution while the next ones recover the local details.

Figura 15 – Modes and frequencies for Rastrigin decomposition

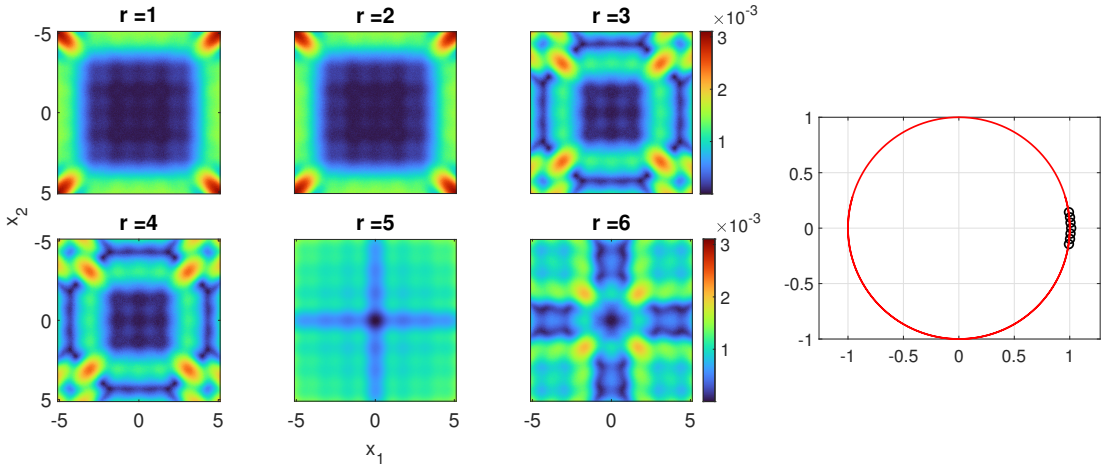

Source: Produced by the author.

For the Griewank field, only two modes are considered, as depicted in Fig. 16. Likewise the previous modal decomposition, the first mode captures the majority of the information, while the second mode adds finer details.

In contrast, the Schaffer field main mode derived from DMD do not accurately describe the behavior of the original field, as displayed in the Fig. 17. This issue is thoroughly examined and discussed in Section 4.4, with hypotheses about the decomposition's failure in this context, along with proposed solutions to deal with this trouble.

Figura 16 – Modes and frequencies for Griewank decomposition.

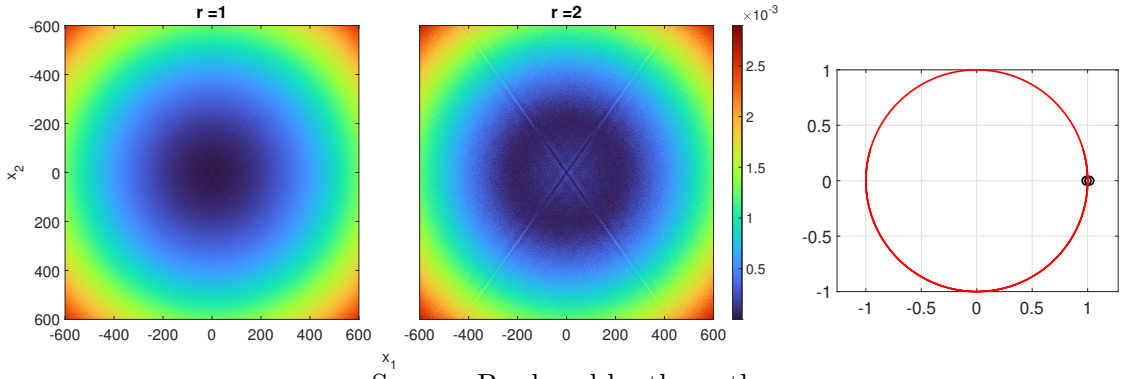

Source: Produced by the author.

Figura 17 – Modes and frequencies for Schaffer N.2 decomposition.

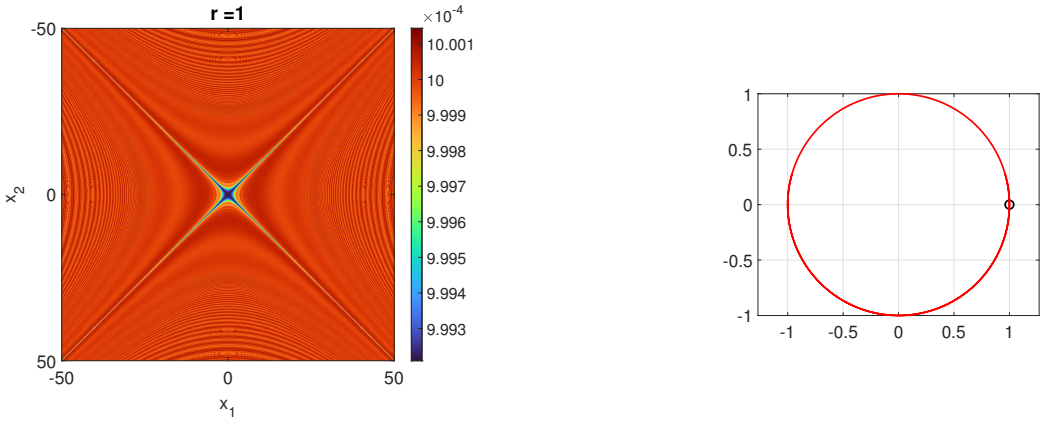

Source: Produced by the author.

About the analytical diffusion field for the cooling plate, the two modes taken are outlined in the Fig. 18. These modes represent properly the field evolution, as further proven in the next section.

Figura 18 – Modes and frequencies for the temperature field decomposition

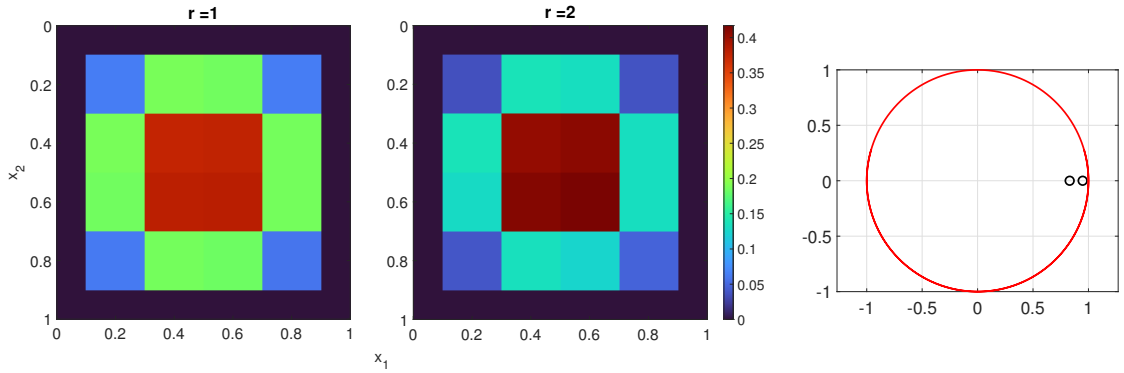

Source: Produced by the author.

The modal decomposition for the experimental field is shown in the Fig. 19, where it is verified that all modes are similar. The frequencies are represented by their respective

colors, so that the frequencies for the red component of the thermal image are stated as red circles in the complex plane, what extend for the green and blue components as well.

Figura 19 – Modes and frequencies for the experimental field decomposition.

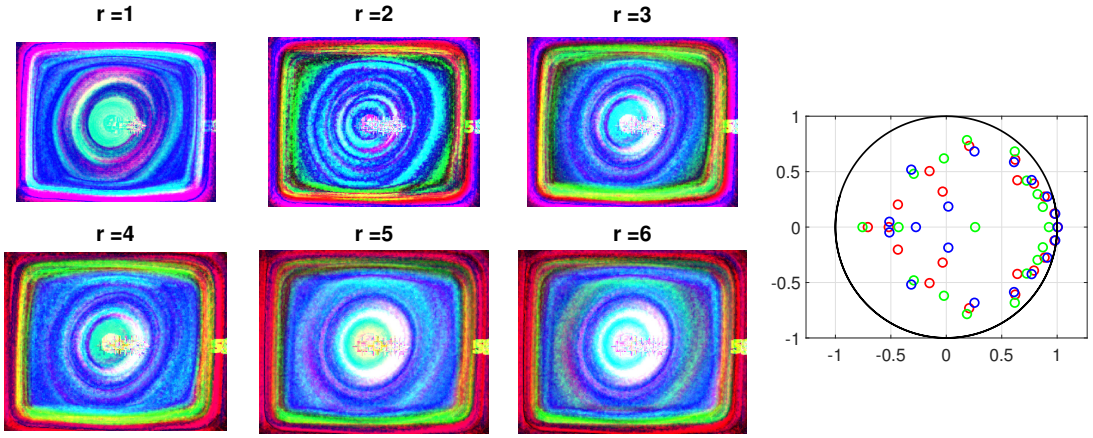

Source: Produced by the author.

An important aspect to highlight is that the eigenvalues of all the dynamical fields presented here lie within the unit circle in the complex plane. Since these fields are discrete, this indicates that the systems are stable.

4.4. COMPARISON BETWEEN ORIGINAL AND RECONSTRUCTED DATA

This section allows an qualitative overview of the decomposition accuracy by comparing the original fields with the reconstructed ones. Likewise, an previous analysis about the truncation step influence on the reconstruction effectiveness is furnished.

Starting from the optimization benchmark fields, the Ackley field reconstruction is stated in the Fig. 20, where the first row is the original field, the second one is its noised version. The third row contains a reconstruction with one mode, showing that just one mode is not enough to get a good reconstruction. Meanwhile, the fourth row proven that nine mode is already capable of generating a good reconstruction. Adding even more modes, we reach the reconstruction with 19 modes placed in the fifth row, resulting an even better reconstruction. However, considering the dimensionality reduction goal, just nine modes produce a result very close to the original field with significantly dimensionality reduction, corroborating the previous singular values analysis.

Figura 20 – Time instants comparison between original and reconstructed data for the Ackley dynamical field. The first row contains the original field, the second one its version added by 10% gaussian noise. The third accomodate the reconstruction with one mode for truncation, the fourth with nine modes, while the fifth comprehend 19 modes. Whereas, the three collumns, represent three instants, the 1^{st}, the 50^{th}, and the 100^{th}

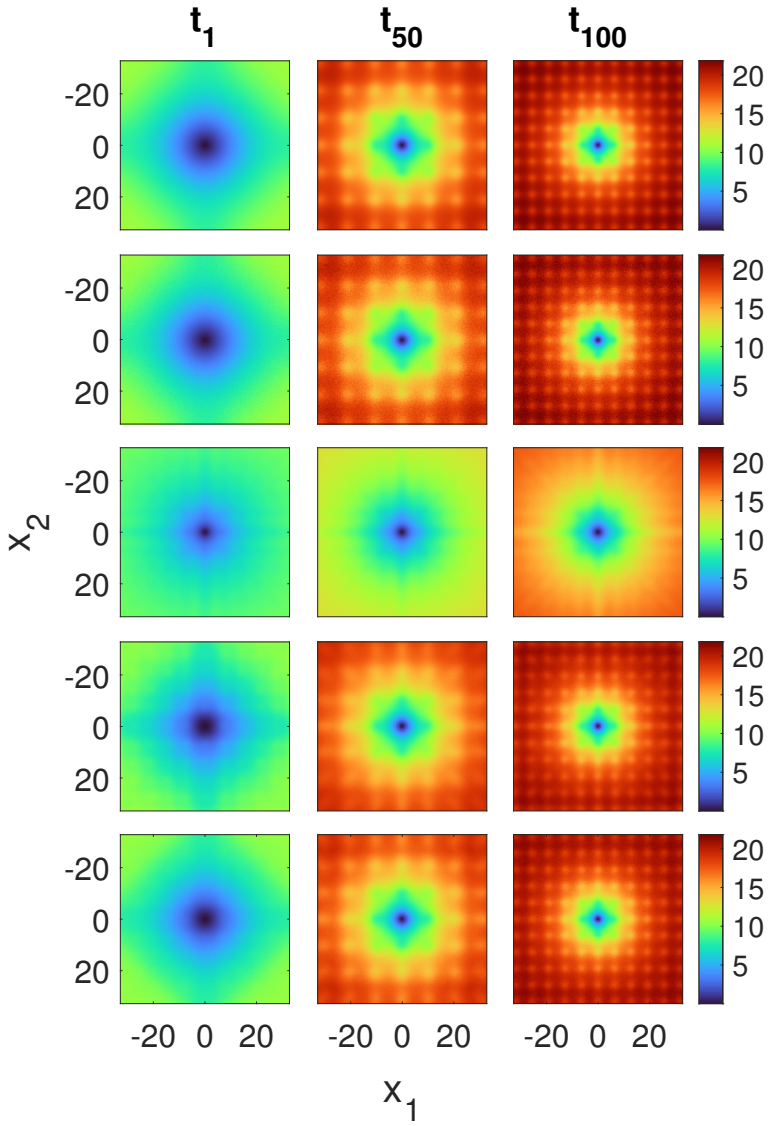

Source: Produced by the author.

The next figures follow the same pattern with first row being the original field by means of comparison, the second row a noised version and finally the last three rows a comparison between three levels of truncation assumed for the reconstruction.

The Rastrigin reconstruction has a bad performance for just one mode, what is seen by the time instants in the third row of Fig. 21. Increasing the truncation limit, with six modes the reconstruction is almost good (fourth row of Fig. 21), and with seven modes the reconstruction is really close to the original field, what is demonstrated by the visual

comparison of the fifth row with the first row of the Fig. 21. Again, the visualization is in line with the singular values study.

Figura 21 – Time instants comparison between original and reconstructed data for the Rastrigin dynamical field. The first row contains the original field, the second one its version added by 10% gaussian noise. The third accommodate the reconstruction with one mode for truncation, the fourth with six modes, while the fifth comprehend seven modes. Whereas, the three columns, represent three instants, the 1^{st}, the 50^{th}, and the 100^{th}

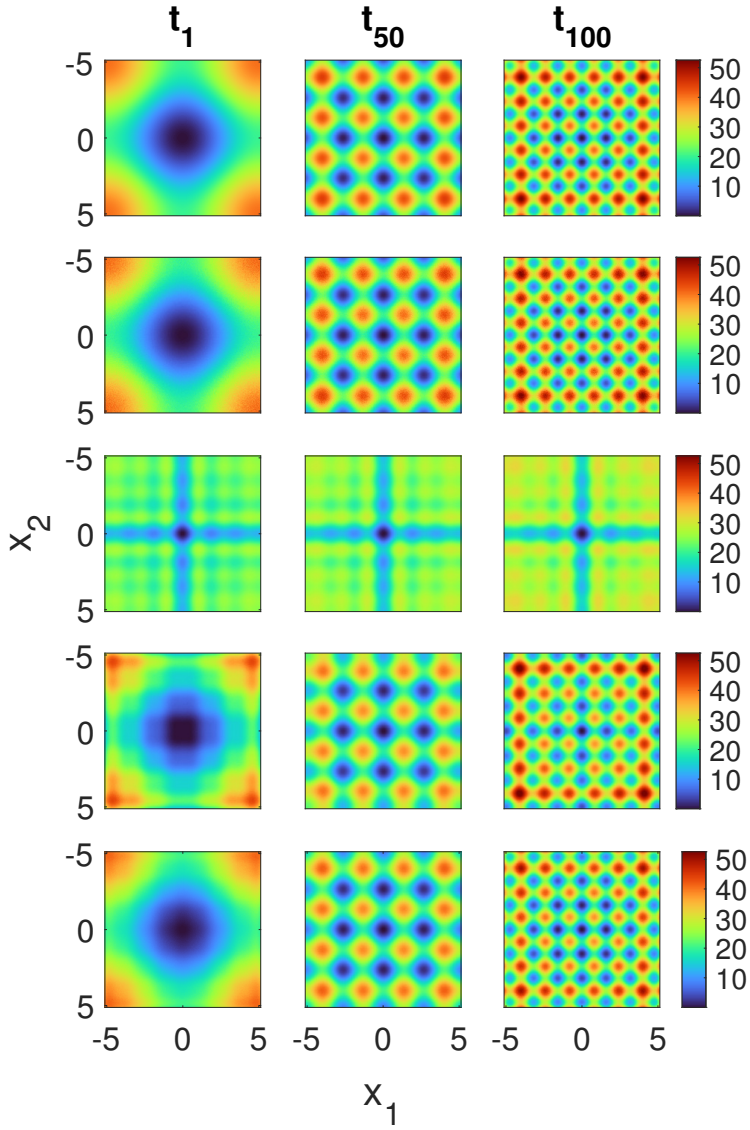

Source: Produced by the author.

Meanwhile, the reconstruction with only two modes (fourth row of Fig. 22) is as good as with 15^{th} modes (fifth row of Fig. 22) for the Griewank field, and significantly better than with just one mode. Thus, the truncation previously chosen confirmed to be a good choice.

Figura 22 – Time instants comparison between original and reconstructed data for the Griewank dynamical field. The first row contains the original field, the second one its version added by 10% gaussian noise. The third accommodate the reconstruction with one mode for truncation, the fourth with two modes, while the fifth comprehend 15 modes. Whereas, the three columns, represent three instants, the the 1^{st}, the 50^{th}, and the 100^{th}

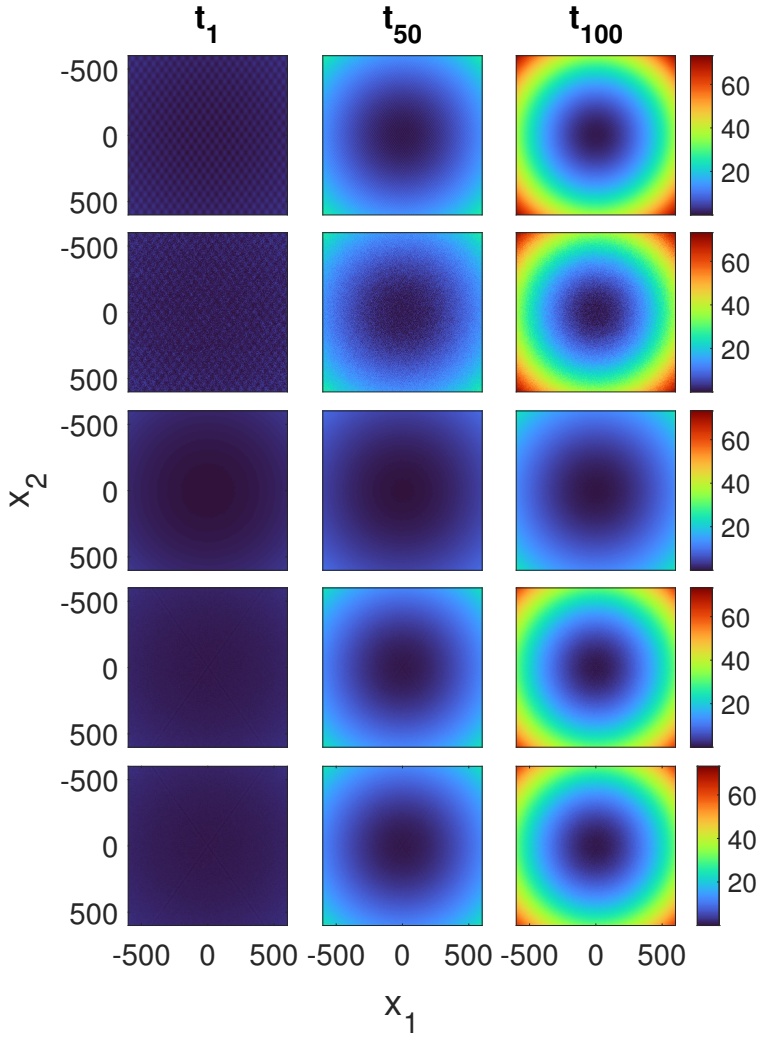

Source: Produced by the author.

Nevertheless, the Schaffer N.2 field could not be well recovered, either with one, ten, or even 100 modes, as can be seen in the Fig. 23. An hypothesis is that DMD has difficulties to deal with this function characteristic discontinuities, once they translates into sparse matrices, demanding SVD and eigendecomposition requires a special treatment. Some alternatives for the exact DMD algorithm has been gaining attention to offer a more robust procedure. The BOP-DMD (Bagging, Optimized Dynamic Mode Decomposition) uses statistical bagging methods to produce an ensemble of DMD models instead of just one, whose output metrics improve the result quality (Sashidhar; Kutz, 2022). Another

modification is proposed by (Askham; Kutz, 2018), allowing to collect unevenly spaced sample times by associating a variable projection method to DMD. There is a broad of others possibilities that have been proposed to deal with DMD limitations, among them the promising extended DMD (Kutz *et al.*, 2016).

Figura 23 – Time instants comparison between original and reconstructed data for the Schaffer N.2 dynamical field. The first row contains the original field, the second one its version added by 10% gaussian noise. The third accommodate the reconstruction with one mode for truncation, the fourth with 10 modes, while the fifth comprehend 100 modes. Whereas, the three columns, represent three instants, the the 1^{st}, the 50^{th}, and the 100^{th}

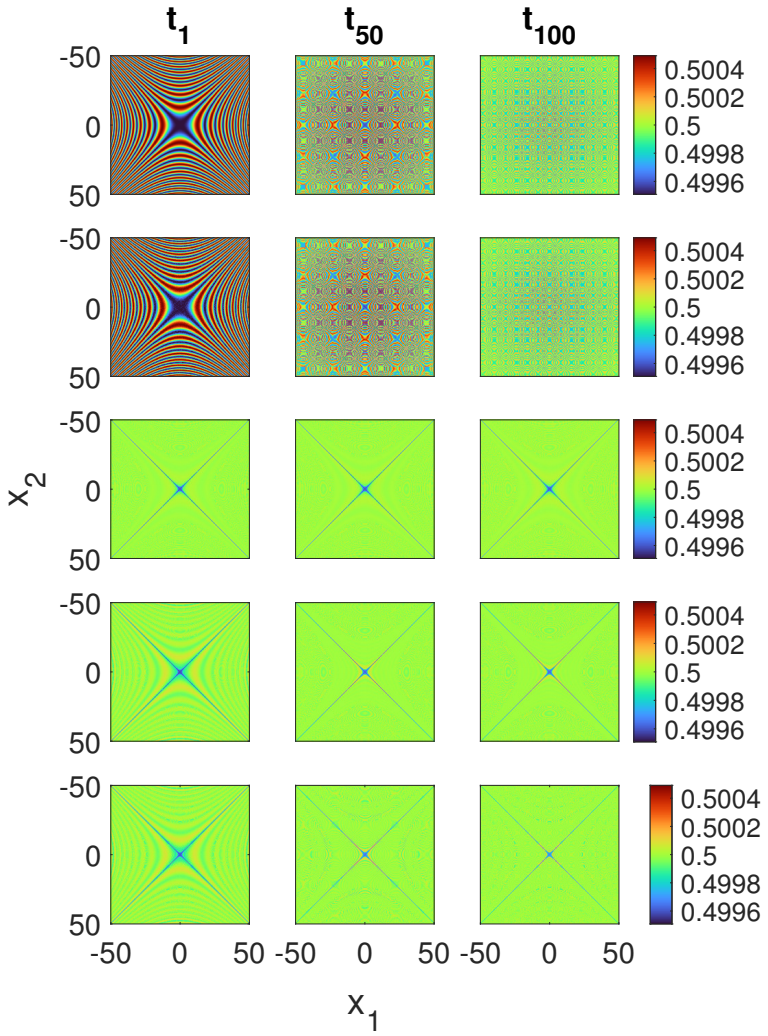

Source: Produced by the author.

Relatively to the field generated by the analytical solution of the cooling plate, an additional panel is stated, showing also the coarsening step described previously. Thus, the Fig. 24 displays the analytical solution of the cooling plate in the first row, the solution with spatial bad sampling in the second row, followed by its noised version with 10%

Gaussian white noise in the third row. Two reconstructions are presented, applying only two modes and using 11 modes for truncation, in the fourth and fifth rows respectively. Notice that two modes is already enough to produce a reconstruction really similar to the original coarsened field. Although, choosing more modes seems also capture noise information, verified by comparing third and fifth rows of the Fig. 24.

Figura 24 – Time instants comparison between original and reconstructed data for the Heat dynamical field. The first row contains the original field, the second one its version sampled with a 10:1 rate in space, and the third enclose represent this field added by 10% gaussian noise. The fourth accommodate the reconstruction with two mode for truncation, while the fifth comprehend 11 modes. Whereas, the three columns, represent three instants, the the 1^{st}, the 50^{th}, and the 100^{th}

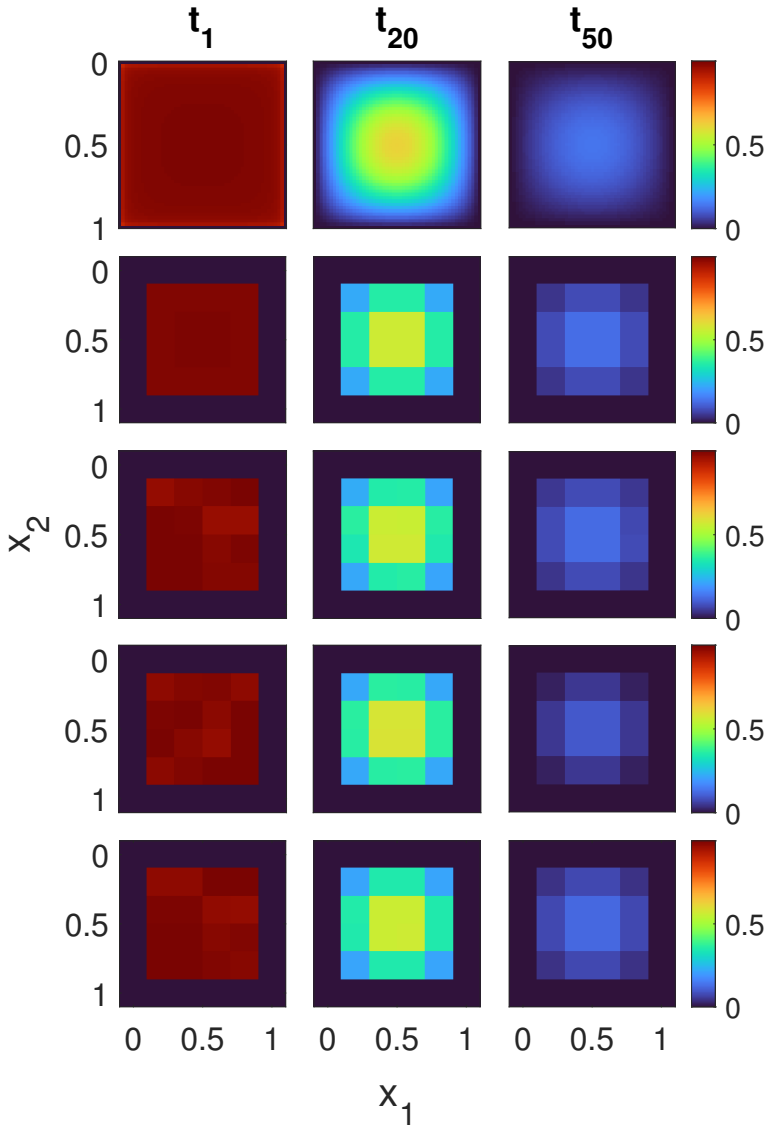

Source: Produced by the author.

The result for reconstruction of experimental field using three layers (RGB) is

exposed in the Fig. 25 using a normalized scale. Notice that red and blue components are well recovered, while the green one is not. A possible reason for this problem is poor sampling in the time, which can be overcome by increasing the sampling rate. Another possibility is a DMD difficulty in deal with sparse matrices, once the green component of the field is restricted to a small region. To handle with this setback, some recent modifications of DMD like the previously presented Bagging, Optimized DMD or Variable Projection Method DMD can be tested. Further, from a pre-processing perspective, exploring the conversion of RGB (Red, Green, Blue) data into the HSV (Hue, Saturation, Value) can be a valuable alternative to explore for improving reconstruction.

Figura 25 – Time instants comparison between original and reconstructed data for the experimental temperature field. The first row contains the original field. Meanwhile, the second one accommodate the reconstruction. Whereas, the three columns, represent three instants, the the 1^{st}, the 50^{th}, and the 100^{th}

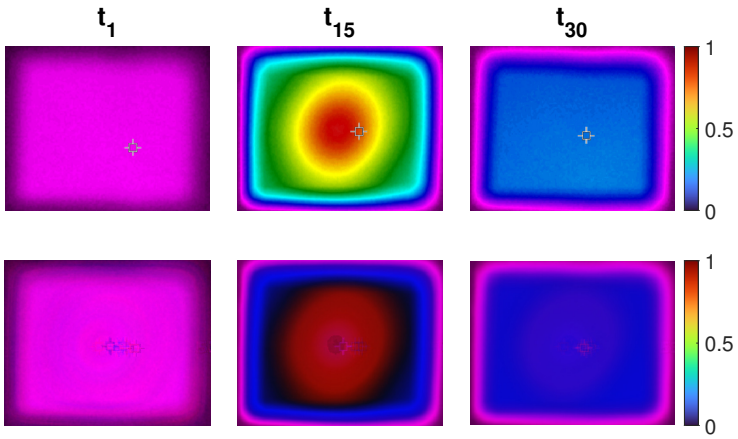

Source: Produced by the author.

4.5. TRUNCATION INFLUENCE ON RECONSTRUCTION THROUGH SIMILARITY ANALYSIS

Despite the visual inspection providing an interesting comparison between original and reconstructed data, also a quantitative perspective is desired (Golub; Loan, 2013). To handle this need, the similarity of the two matrices is computed using the cosine of the angle between them,

$$\cos(\theta) = \frac{\mathbf{v_1} \cdot \mathbf{v_2}}{|\mathbf{v_1}||\mathbf{v_2}|} , \tag{4.6}$$

Figura 26 – Truncation analysis through similarity of the Ackley (a), Rastrigin (b), Griewank (c), Schaffer N.2 (d) fields and for the analytical temperature field of the cooling aluminum plate (e).

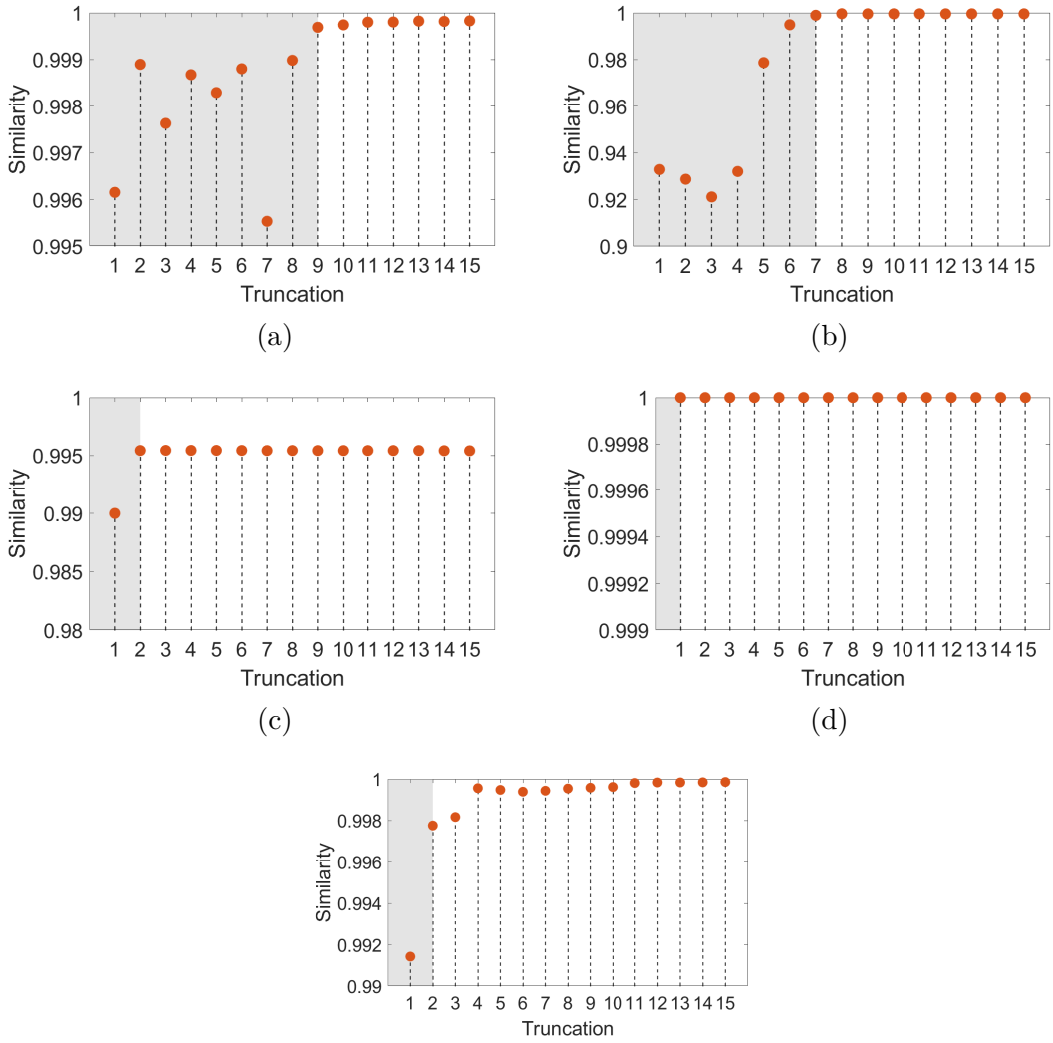

Source: Produced by the author.

where $\mathbf{v_1}$ represent the $\mathbf{X}$ matrix stretched into a single vector, while the $\mathbf{v_2}$ is the stretched version of the reconstructed matrix $\mathbf{X_r}$. As it is a cosine measure, the closer to one the more similar. Using the similarity tool, an exploration of the truncation influence in the quality of the reconstruction are realized.

For the analytical fields, the results are exposed in the Fig. 26, while for the experimental data is in the Fig. 27, splitted in its three components (RGB). The truncation regions assumed are again highlighted in light gray.

The inspection of the results allows proof of the previous analysis, confirming the truncation levels chosen. An interesting aspect is that the Griewank function reconstruc-

Figura 27 – Truncation analysis through similarity of the red (a), green (b), and blue (c) components of the experimental field.

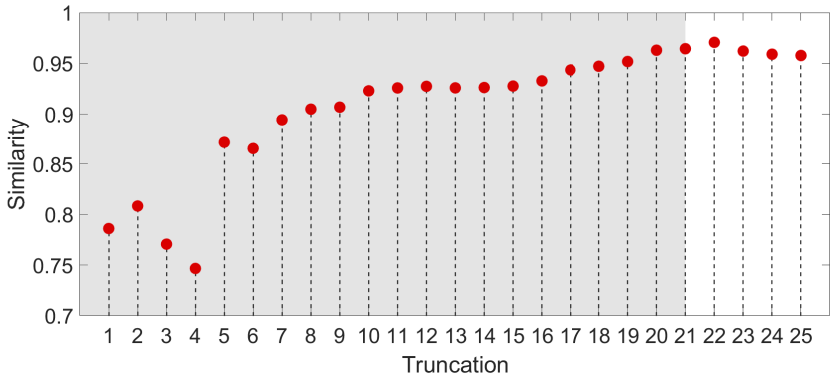

(a)

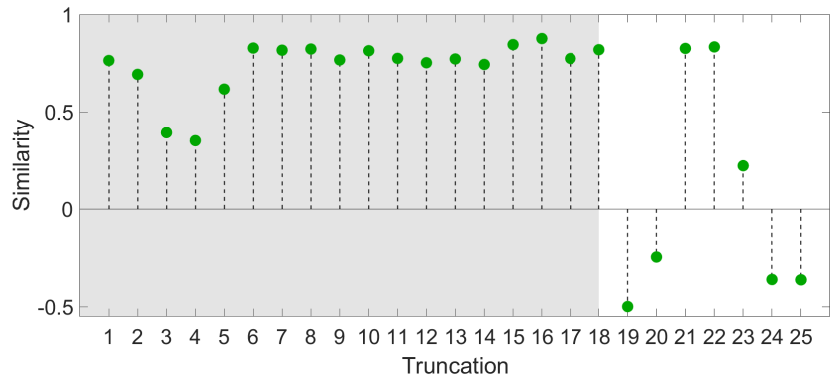

(b)

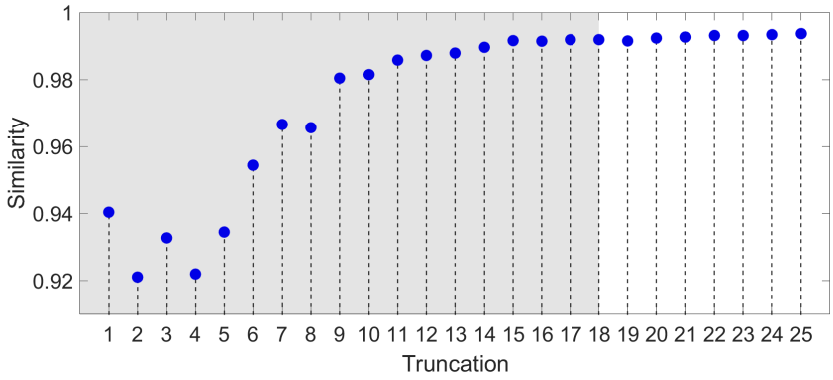

(c)

Source: Produced by the author.

tion does not seem to reach similarity one even in a truncation long horizon, reflecting the exact DMD can not capture some subtle details. Another point to mention is that even with a bad reconstruction, proven by the instant visualization, the Schaffer N.2 field similarity is really close to one, which reveals similarity alone is not useful and must be sparingly used, so that a suggestion to improve analysis is to verify more metrics like the statistical measures for the difference between the original and reconstruction field,

to quote media and variance. A last interesting result to point out is the unstable behavior of the green component similarity concerning the truncation, which reflects the poor reconstruction of this color spectra already seen.

5 FINAL REMARKS

This chapter is splitted in three sections: the Section 5.1 summarizes the conclusions from this dissertation, the Section 5.2 presents the scientific contributions during master's course, while the Section 5.3 delineates potential next steps for this research.

5.1. CONCLUSIONS

This dissertation explored the application of Dynamic Mode Decomposition (DMD) in analyzing nonlinear dynamical systems, emphasizing its ability in extracting and reconstructing spatio-temporal patterns with reduced dimensionality. The investigation initiated with the theoretical foundations, passed through the algorithm description, and reached practical applications, where the DMD power was challenged.

The literature review provided a theoretical background for the Koopman operator and its approximation through the DMD for dealing with complex dynamical systems using just data. The development of the DMD reconstruction algorithm was also explained in detail.

Four benchmark functions from optimization problems were employed to test the DMD algorithm, generating complex dynamic field data. The results highlighted DMD's strengths in reconstructing these fields with high accuracy, even in the presence of noise emulating experimental disturbances. This previous analysis allows conducting DMD for a testing with physical applications, where data may be also imperfect or incomplete.

A part of the research was dedicated to the heat diffusion phenomenon in a homogeneous, isotropic flat plate. For this application along with noise, also a spatial poor sampling is applied emulating real situations, with disturbances and limited sensoring. The results shows that DMD algorithm again successfully recovered the dynamic temperature field.

Furthermore, finally, the experimental data collected from the heat diffusion experiment demonstrated the practical applicability of DMD. The ability to extract modes, frequencies, and an approximation of the Koopman operator from the experimental data shed light in the direction of real system identification and control.

In verifying the success of the DMD algorithm, it was essential to verify both the similarity and the visualization of the reconstructed fields. Accurate reconstruction

requires not only quantitative metrics but also qualitative visual assessments to confirm that the reconstructed fields will closely resemble the original data. This dual criterion is crucial to ensure the captured modes accurately represent the underlying dynamics of the system.

DMD has proven to be a powerful tool for dimensionality reduction, significantly simplifying complex datasets. For each field analyzed, only a small number of modes were necessary to achieve accurate reconstructions. For instance, the heat diffusion field was effectively captured using just a few dominant modes, illustrating the efficiency of DMD in reducing the dimensionality of high-dimensional datasets without loosing the main field information.

However, some limitations were encountered and deserves careful attention. The accuracy of the DMD algorithm was found to be highly dependent on the quality of input data, so that a rigorous pre-processing step is required, by pointing results limitations and requirements based on physical understanding. Additionally, the computational cost of DMD can be significant, especially for very high-dimensional datasets. Another care that must be taken is related to sparse matrices and surfaces with sharp peaks, where DMD can not capture well the dynamics and variations of exact DMD could be a good suggestion to surpass this concern.

Overall, the findings of this dissertation confirm the promise of DMD as a valuable tool for studying dynamic systems, particularly those with unknown or partially known governing equations. The method's ability to provide high-fidelity reconstructions with reduced dimensionality positions it as a powerful approach for application in various fields of engineering and beyond.

5.2. SCIENTIFIC PRODUCTION

The development of this research allows the following productions.

- Presentation of "Dynamic Mode Decomposition: A Powerfull Data-Driven Modeling Tool"in the Simpósio PPGEM 2023 - Ilha Solteira/SP;
- Presentation of "Reconstrução de Campos Dinâmicos via Decomposição em Modos Dinâmicos"in the VIII ERMAC (Encontro Regional de Matemática Aplicada e Computacional) - Regional 9 - Ilha Solteira/SP;

- Registration of the software ”DynaMoDE - Dynamic Mode Decomposition Engine”in Intituto Nacional de Propriedade Intelectual (INPI).

The most recent results are also generating ongoing productions.

5.3. FUTURE DIRECTIONS

Some future directions are proposed for the following of this research:

- The application of new variant of DMD, like BOP-DMD is an interesting field in direction of improve the method robustness;
- An inherent intention that also emerges from this promising capabilities relies on comparing the DMD methodology with another data-driven methods such as Karhunen-Loève Expansion (KLE);
- Likewise, the exploration of the DMD capabilities of diagnosis, prediction and control is a further aim.

REFERENCES

ALVES, C. D. *et al.* Horizon extraction using absolute seismic phase obtained by unwrapping techniques. **Journal of Applied Geophysics**, Amsterdam, v. 218, p. 105198, 2023.

ARAUJO, L. S. **DMD Reconstruction Code**. GitHub, 2024. Disponível em: https://github.com/lucas-simon-araujo/DMD-Reconstruction.

ASKHAM, T.; KUTZ, J. N. Variable projection methods for an optimized dynamic mode decomposition. **SIAM Journal on Applied Dynamical Systems**, Philadelphia, v. 17, n. 1, p. 380–416, 2018.

BARROS, G. F.; CORTES, A. M. A.; COUTINHO, A. L. G. A. Dynamic mode decomposition for density-driven gravity current simulations. In: **Proceedings of the XLI Ibero-Latin-American Congress on Computational Methods in Engineering**. Foz do Iguaçu, Brazil: [s.n.], 2020.

BARROS, G. F. *et al.* Dynamic mode decomposition in adaptive mesh refinement and coarsening simulations. **Engineering with Computers**, Berlin, v. 38, n. 5, p. 4241–4268, 2022.

BRUNTON, S. L.; KUTZ, J. N. **Data-Driven Science and Engineering : Machine Learning, Dynamical Systems, and Control**. [S.l.]: Cambridge University Press, 2019.

BUDIŠIĆ, M.; MOHR, R.; MEZIĆ, I. Applied Koopmanism. **Chaos: An Interdisciplinary Journal of Nonlinear Science**, Huntington, v. 22, n. 4, p. 047510, 2012.

Cunha Jr., A. **Modeling and Uncertainty Quantification in the Nonlinear Stochastic Dynamics of Horizontal Drillstrings**. Tese (D.Sc. Thesis) — PUC-Rio, Rio de Janeiro, Brazil, 2015.

Cunha Jr., A.; SOIZE, C.; SAMPAIO, R. Computational modeling of the nonlinear stochastic dynamics of horizontal drillstrings. **Computational Mechanics**, Heidelberg, v. 56, n. 5, p. 849–878, 2015.

EMERICK, A. A. Deterministic ensemble smoother with multiple data assimilation as an alternative for history-matching seismic data. **Computational Geosciences**, Cham, v. 22, n. 5, p. 1175–1186, 2018.

FACCHINETTI, M.; LANGRE, E. D.; BIOLLEY, F. Coupling of structure and wake oscillators in vortex-induced vibrations. **Journal of Fluids and Structures**, Paris, v. 19, n. 2, p. 123–140, 2004.

FREITAS, R. S. M. *et al.* An encoder-decoder deep surrogate for reverse time migration in seismic imaging under uncertainty. **Computational Geosciences**, Cham, v. 25, n. 3, p. 1229–1250, 2021.

GOLUB, G. H.; LOAN, C. F. V. **Matrix Computations**. 4th. ed. [S.l.]: Johns Hopkins University Press, 2013.

GU, M. *et al.* Probabilistic forecast of nonlinear dynamical systems with uncertainty quantification. **Physica D: Nonlinear Phenomena**, Amsterdam, v. 457, p. 133938, 2024.

KAISER, E.; KUTZ, J. N.; BRUNTON, S. L. Data-driven discovery of Koopman eigenfunctions for control. **Machine Learning: Science and Technology**, Bristol, v. 2, n. 3, p. 035023, 2021.

KOOPMAN, B. O. Hamiltonian systems and transformation in Hilbert space. **Proceedings of the National Academy of Sciences**, Washington, D.C., v. 17, n. 5, p. 315–318, 1931.

KURUSHINA, V.; PAVLOVSKAIA, E. Fluid nonlinearities effect on wake oscillator model performance. **MATEC Web of Conferences**, Les Ulis, v. 148, p. 04002, 2018.

KUTZ, J. N. *et al.* **Dynamic Mode Decomposition: Data-Driven Modeling of Complex Systems**. [S.l.]: Society for Industrial and Applied Mathematics, 2016.

KUTZ, J. N.; PROCTOR, J. L.; BRUNTON, S. L. Applied koopman theory for partial differential equations and data-driven modeling of spatio-temporal systems. **Complexity**, *[S. l.]*, v. 2018, p. e6010634, 2018.

LI, C. Y. *et al.* Koopman analysis by the dynamic mode decomposition in wind engineering. **Journal of Wind Engineering and Industrial Aerodynamics**, North York, v. 232, p. 105295, 2023.

LIENHARD V, J. H.; LIENHARD IV, J. H. **A Heat Transfer Textbook**. 6th. ed. Cambridge, MA: Phlogiston Press, 2024.

LOBO, D. *et al.* On the stochastic bit–rock interaction disturbances and its effects on the performance of two commercial control strategies used in drill strings. **Mechanical Systems and Signal Processing**, Eindhoven, v. 164, p. 108229, 2022.

LOPES, G. J. V. **Contributions to the investigation of the nonlinear dynamics of immersed slender structures: reduced-order model analysis and their advantages.** Tese (D.Sc. Thesis) — Universidade de São Paulo, 2022.

LOPES, V. G.; PETERSON, J. V. L. L.; Cunha Jr., A. Nonlinear characterization of a bistable energy harvester dynamical system. In: BELHAQ, M. (Ed.). **Topics in Nonlinear Mechanics and Physics**. [S.l.]: Springer Singapore, 2019. p. 71–88.

MEZIĆ, I. Spectral Properties of Dynamical Systems, Model Reduction and Decompositions. **Nonlinear Dynamics**, London, v. 41, n. 1, p. 309–325, 2005.

MEZIĆ, I. Analysis of fluid flows via spectral properties of the Koopman operator. **Annual Review of Fluid Mechanics**, San Mateo, v. 45, n. 1, p. 357–378, 2013.

MEZIĆ, I.; BANASZUK, A. Comparison of systems with complex behavior. **Physica D: Nonlinear Phenomena**, Amsterdam, v. 197, n. 1–2, p. 101–133, 2004.

NORENBERG, J. P. *et al.* Nonlinear dynamics of asymmetric bistable energy harvesters. **International Journal of Mechanical Sciences**, Oxford, v. 257, p. 108542, 2023.

PING, H. *et al.* Dynamic mode decomposition based analysis of flow past a transversely oscillating cylinder. **Physics of Fluids**, Huntington, v. 33, n. 3, p. 033604, 2021.

PROCTOR, J. L.; BRUNTON, S. L.; KUTZ, J. N. Dynamic mode decomposition with control. **SIAM Journal on Applied Dynamical Systems**, Philadelphia, v. 15, n. 1, p. 142–161, 2016.

REIS, A. S. *et al.* Unravelling COVID-19 waves in Rio de Janeiro city: Qualitative insights from nonlinear dynamic analysis. **Infectious Disease Modelling**, Toronto, v. 9, n. 2, p. 314–328, 2024.

RITTO, T. G.; AGUIAR, R. R.; HBAIEB, S. Validation of a drill string dynamical model and torsional stability. **Meccanica**, London, v. 52, n. 11–12, p. 2959–2967, 2017.

RITTO, T. G. *et al.* Fuzzy logic control of a drill-string. In: **Proceedings of the XXX Iberian-Latin American Congress on Computational Methods in Engineering**. [S.l.: s.n.], 2009.

ROWLEY, C. W. *et al.* Spectral analysis of nonlinear flows. **Journal of Fluid Mechanics**, Cambridge, v. 641, p. 115–127, 2009.

SAMPAIO, R.; WOLTER, C. Bases de karhunen-loève: aplicações à mecânica dos sólidos. In: . São Carlos, SP, Brazil: [s.n.], 2001.

SASHIDHAR, D.; KUTZ, J. N. Bagging, optimized dynamic mode decomposition for robust, stable forecasting with spatial and temporal uncertainty quantification. **Philosophical Transactions of the Royal Society A: Mathematical, Physical and Engineering Sciences**, Londres, v. 380, n. 2229, 2022.

SAVI, M. A. **Dinâmica Não-linear e Caos**. Brazil: E-Paper, 2017.

SCHMID, P. J. Dynamic mode decomposition of numerical and experimental data. Cambridge, v. 656, p. 5–28, 2010.

SCHMID, P. J. Dynamic mode decomposition and its variants. **Annual Review of Fluid Mechanics**, San Mateo, v. 54, n. 1, p. 225–254, 2022.

SCHMID, P. J. *et al.* Applications of the dynamic mode decomposition. **Theoretical and Computational Fluid Dynamics**, London, v. 25, n. 1-4, p. 249–259, 2011.

SILVA, C. W. **Modeling of Dynamic Systems with Engineering Applications**. 2. ed. [S.l.]: CRC Press, 2022.

SPALL, J. C. **Introduction to Stochastic Search and Optimization: Estimation, Simulation, and Control**. [S.l.]: Wiley, 2003.

STROGATZ, S. **Nonlinear Dynamics and Chaos with Applications to Physics, Biology, Chemistry, and Engineering**. 2nd. ed. [S.l.]: Westview Press, 2014.

VIGUERIE, A. *et al.* Data-driven simulation of Fisher–Kolmogorov tumor growth models using dynamic mode decomposition. **Journal of Biomechanical Engineering**, New York, v. 144, n. 12, p. 121001, 2022.

WANG, D. *et al.* Bifurcation analysis of vortex-induced vibration of low-dimensional models of marine risers. **Nonlinear Dynamics**, Bristol, v. 106, n. 1, p. 147–167, 2021.

WILLIAMS, M. O.; KEVREKIDIS, I. G.; ROWLEY, C. W. A data–driven approximation of the Koopman operator: Extending dynamic mode decomposition. **Journal of Nonlinear Science**, New York, v. 25, n. 6, p. 1307–1346, 2015.